A phenomenological model for microstructure-dependent inelasticity in shape-memory alloys

D. Grandi[a,*], U. Stefanelli[b]

[a] *Faculty of Mathematics, University of Vienna, Oskar-Morgenstern-Platz 1, A-1090 Vienna, Austria*

[b] *Faculty of Mathematics, University of Vienna, Oskar-Morgenstern-Platz 1, A-1090 Vienna, Austria*

Abstract

Fatigue and degradation in shape-memory alloy response is a crucial concern for a variety of innovative applications. Under cyclic loadings, these materials generally experience permanent inelastic deformations. The onset of plasticization is known to be very sensitive to the microstructure of the polycrystalline specimen.

Moving from recent experimental findings [9, 11], we present a phenomenological model for permanent inelastic effects in shape-memory alloys taking into account the polycrystalline microstructure. In particular, the mechanical response under cyclic loadings is assumed to be dependent both on the degree of crystallization and the mean crystal grain size. Formulated within the variational frame of Generalized Standard Materials, the model consists in an extension of the model in [5] to the microstructure-dependent parameter case. The mathematical setting is discussed and numerical simulations showing the capability of the model to reproduce experiments are presented.

Keywords: Microstructures, fatigue, cyclic loading, constitutive behavior, variational calculus

*Corresponding author

Email addresses: diego.grandi@univie.ac.at (D. Grandi), ulisse.stefanelli@univie.ac.at (U. Stefanelli)

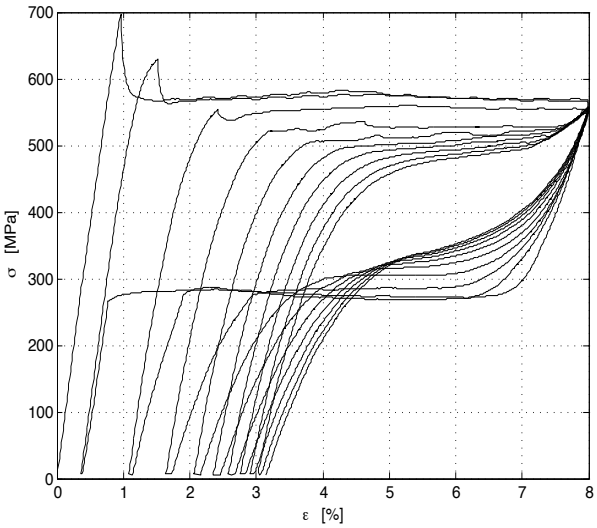

Figure 1: Cyclic loading response in NiTi [10].

1. Introduction

Shape Memory Alloys (SMAs) are usually referred to as *active* materials for considerably large strains can be *activated* by either thermal, mechanical, or magnetic stimuli [15, 23]. The functional properties of Shape Memory Alloys (SMAs) are at the basis of a large range of innovative applications such as sensors, actuators, and MEMS in a number of different fields from Biomechanics and Medical Engineering, to Seismic and Aerospace Engineering [13]. Correspondingly, the experimental investigation and the constitutive material modeling for SMAs has attracted a constantly increasing attention in the last decades.

A emerging technological issue is that of tailoring the SMA manufacturing processes in order to improve their functional properties. In particular, one is interested in predicting and possibly controlling the accumulation of fatigue and degradation effects under cyclic loading regimes [16, 29, 31]. Figure 1 reports the experimental stress-strain response of a NiTi wire subject to a stress-driven uniaxial cyclic tension test. Pseudoelastic loops show an increasing level of permanent inelasticity which eventually saturates. Due to its applicative relevance, the effective modelization of permanent inelastic effects has recently

attracted considerable attention [5, 8, 22, 28, 33, 34, 24, 20, 21, 35, 36].

The polycrystalline texture of the material has a strong influence on the onset of plasticization [17, 30, 37]. In the recent series of papers [9, 10, 11, 12] the Authors provide experimental evidence of the influence of the polycrystalline microstructure on the functional behavior on fatigue and degradation in SMAs. A commercial NiTi wire is heat treated by electric pulses in such a way to induce recrystallization from the amorphous phase as well as crystal-grain coarsening. Then, the pseudoelastic response is tested and the microstructure is analyzed by transmission electron microscopy. On the one hand, in the completely recrystallized situation, it is observed that pseudoelastic effects are favored under comparably large mean crystal-grain sizes. On the other hand, as grains grow larger fatigue effects become apparent. As such, one is interested in identifying an *optimal* microstructure which at the same time allows for a relevant martensitic reorientation effect (in terms of the size of the corresponding transformation strain) while controlling the accumulation of fatigue and degradation. For the specific experimental situation of [10] such an optimal microstructure corresponds to a mean grain-size in the 20-50 nm range.

The purpose of this work is to propose a phenomenological model capable of describing the observed fatigue and degradation effects under cyclic loadings in connection with the polycrystalline microstructure of the material. Our starting point is a recent model for the inelastic behavior of SMAs proposed in [5]. This model, which we refer to as the ARS model throughout, is in turn built on the original framework by Souza, Mamiya, and Zouain [32] and Auricchio and Petrini [2, 3, 4], see the recent review [18]. Formulated within the classical frame of Generalized Standard Materials, the ARS model is a phenomenological model featuring the rate-independent evolution of the inelastic and plastic strains of the body as the relevant internal variables. Despite its relative simplicity in terms of number of material parameters, the ARS model has proved very effective in describing fatigue accumulation and degradation effects [5], while being robust with respect to discretizations and approximations, and amenable to a satisfactory mathematical

treatment [14].

Our strategy in order to extend the ARS model to microstructure dependencies is that of including two additional internal variables, the *proportion of crystallized material* and the *mean crystal-grain radius*. This will be done by choosing some specific form of microstructural dependence of the original parameters in the ARS model.

The novelty of this paper is twofold. From the one hand, after recalling the basic traits of the original ARS model (Section 2) we present its detailed analysis in the uniaxial tension case. This allows us to clarify the role of the various material parameters in the ARS model and to present a new effective strategy in order to calibrate these parameters on the basis of experimental cyclic loading tests (Section 3).

Secondly, we employ the above-mentioned fitting procedure in order to propose the new microstructure-dependent extension of the ARS model (Section 4). The model results from few simple assumptions on the scaling of free energy and dissipation in the material. The extended model still enjoys the remarkable features of the original ARS model. In particular, it can be quite effectively time-discretized in order to obtain numerical simulations. These simulations are in good agreement with the experimental findings of [9, 10, 11, 12].

Before moving on, let us mention some other recent contributions to the modeling of permanent inelastic effects in the super-elastic regime of SMA. Macroscopic models combining pseudoelasticity and thermal strain recovery with the onset of plastic [20] (or viscoplastic [21]) strains have been reported by Hartl and Lagoudas. The proposal of Zaki and Moumni [35, 36] can be counted in the same class of non-crystallographic macro-scale description. Manchiraju and Anderson (2010) proposed a microstructure-based model [24] aiming to describe the interaction between martensitic transformation and plasticity. A micromechanical constitutive model based on crystal plasticity for cyclic deformations has been recently proposed by Yu et al. [33, 34].
In a recent contribution by Barrera, Biscari and Urbano [7] where another modification of the ARS model displaying an evolving elastic domain is considered. The idea here

is to model degradation in thermoelastic cyclic experiments by letting the size of the elastic domains depend on plasticization. Our perspective here is different as we focus on isothermal mechanical cycles instead.

2. The ARS model for permanent inelastic effects

In order to set the stage for our microstructure dependent modelization, let us start by recalling the basic features of the ARS model [5]. As already mentioned, this is an extension of the Souza-Auricchio model [2, 18, 32] to the case of permanent plastic effects. In particular, it is a macro-scale, small-strain model of internal-variable type for polycrystalline specimens.

2.1. State variables

The basic kinematic variable is the linearized strain

$$\boldsymbol{\varepsilon}(\boldsymbol{u}) = \frac{1}{2}(\nabla \boldsymbol{u} + \nabla \boldsymbol{u}^T) \in \mathbb{R}^{3\times 3}_{\text{sym}}$$

where $\boldsymbol{u}$ denotes the displacement vector field and $\mathbb{R}^{3\times 3}_{\text{sym}}$ stands for the space of symmetric 2-tensors in $\mathbb{R}^3$.

Two additional kinematic strain-like variables, the *transformation strain* $\boldsymbol{e}^{\text{tr}}$ and the *plastic strain* $\boldsymbol{q}$, characterize the state of the system. The transformation strain $\boldsymbol{e}^{\text{tr}}$ is defined as the inelastic part of the strain, that is, it fulfills the constitutive relation

$$\boldsymbol{\varepsilon}(\boldsymbol{u}) = \boldsymbol{\varepsilon}^{\text{el}} + \boldsymbol{e}^{\text{tr}}, \tag{2.1}$$

where $\boldsymbol{\varepsilon}^{\text{el}}$, the elastic strain, is a linear function of the stress $\boldsymbol{\sigma}$. The transformation strain $\boldsymbol{e}^{\text{tr}}$ is in turn decomposed as the sum of a *martensitic strain* $\boldsymbol{e}^{\text{m}}$ and a *plastic strain* $\boldsymbol{q}$:

$$\boldsymbol{e}^{\text{tr}} = \boldsymbol{e}^{\text{m}} + \boldsymbol{q}. \tag{2.2}$$

The tensor $\boldsymbol{e}^{\text{tr}}$ corresponds to the inelastic strain associated to the martensitic transformation whereas $\boldsymbol{q}$ is interpreted as the fatigue-induced plasticization strain.

The strains $\boldsymbol{e}^{\mathrm{tr}}$ and $\boldsymbol{q}$ are considered as kinematically independent variables, while $\boldsymbol{e}^{\mathrm{m}}$ is *defined* via (2.2). Relation (2.1) is hence a constitutive relation between independent variables. Both tensors $\boldsymbol{e}^{\mathrm{tr}}$ and $\boldsymbol{q}$ are *symmetric* and *deviatoric*, reflecting the quasi-isovolumetric character of both the martensitic phase transition and the plastic evolution. In particular, we write

$$\boldsymbol{e}^{\mathrm{tr}}, \boldsymbol{q} \in \mathbb{R}^{3\times 3}_{\mathrm{dev}} := \{\boldsymbol{a} \in \mathbb{R}^{3\times 3}_{\mathrm{sym}} \mid \mathrm{Tr}\, \boldsymbol{a} = \boldsymbol{0}\}$$

where $\mathrm{Tr}\, \boldsymbol{a} := \boldsymbol{I} : \boldsymbol{a}$ is the trace of the tensor $\boldsymbol{a}$, $\boldsymbol{I}$ is the identity 2-tensor, and : denotes the standard contraction product.

A basic assumption of the model is the constraint for the transformation strain

$$\|\boldsymbol{e}^{\mathrm{tr}}\| := (\boldsymbol{e}^{\mathrm{tr}} : \boldsymbol{e}^{\mathrm{tr}})^{1/2} \leq \varepsilon_L \tag{2.3}$$

where $\varepsilon_L > 0$ corresponds to the maximal uniaxial strain obtainable via martensitic reorientation. Accordingly, one would be tempted to constrain $\|\boldsymbol{e}^{\mathrm{m}}\|$ rather than $\|\boldsymbol{e}^{\mathrm{tr}}\|$. However, it is empirically seen that the maximum value of $\|\boldsymbol{e}^{\mathrm{tr}}\|$ is very little dependent on the experienced fatigue in comparison with the fatigue-induced residual strain [9, 10, 17]. One hence resorts in constraining the entire inelastic response of the material via (2.3), see [5].

2.2. Energy

The material behavior falls in the class of rate-independent models for Generalized Standard Materials [19]. The evolutive laws are characterized in terms of a (Gibbs) free energy potential and a positively one-homogeneous dissipation (pseudo)potential. The free-energy density is assumed to be

$$\begin{aligned}\Phi(\boldsymbol{\sigma}, \boldsymbol{e}^{\mathrm{tr}}, \boldsymbol{q}) = -\frac{1}{2}\boldsymbol{\sigma} : \mathbb{C}^{-1}\boldsymbol{\sigma} - \boldsymbol{\sigma} : \boldsymbol{e}^{\mathrm{tr}} + \\ + \beta_0(T - M_f)^+\|\boldsymbol{e}^{\mathrm{tr}} - \boldsymbol{q}\| + \frac{h}{2}\|\boldsymbol{e}^{\mathrm{tr}}\|^2 - A\varepsilon^{\mathrm{tr}} : \boldsymbol{q} + \frac{H}{2}\|\boldsymbol{q}\|^2 + I_{\varepsilon_L}(\boldsymbol{e}^{\mathrm{tr}}).\end{aligned} \tag{2.4}$$

Here, $\mathbb{C}$ is the isotropic elasticity tensor

$$\mathbb{C}^{-1}\boldsymbol{\sigma} = \frac{1+\nu}{E}\boldsymbol{s} + \frac{1-2\nu}{3E}\mathrm{Tr}(\boldsymbol{\sigma})\boldsymbol{I}$$

where $\boldsymbol{s} = \boldsymbol{\sigma} - \mathrm{Tr}(\boldsymbol{\sigma})\,\boldsymbol{I}/3$ is the *deviatoric* stress tensor, and ν and E are respectively the Poisson ratio and the Young modulus. Note that the same elastic response is assumed for both austenite and martensite for simplicity (see [6] for a generalization). The thermomechanical coupling term features the occurrence of the quantity

$$\beta_0(T - M_f)^+ = \beta((T - M_f) \vee 0)$$

($\vee$ denotes the maximum) where T denotes the absolute temperature, M_f is the so-called *martensitic finish temperature* (below which the martensitic phase is stable at zero stress). As we restrict here to the isothermal situation, we shall simplify the notation by using systematically the symbol β as a place holder for $\beta_0(T - M_f)^+$. The last term in the free energy enforces the constraint on the transformation strain through the *indicator function*

$$I_{\varepsilon_L}(\boldsymbol{e}^{\mathrm{tr}}) := \begin{cases} 0 & \text{if } \ \|\boldsymbol{e}^{\mathrm{tr}}\| < \varepsilon_L, \\ +\infty & \text{otherwise.} \end{cases}$$

Finally, h, H, A are positive hardening-like parameters.

We shall assume form the very beginning the *convexity condition*

$$hH > A^2. \tag{2.5}$$

This condition entails that the Gibbs free energy density is uniformly convex in its variables $(\boldsymbol{e}^{\mathrm{tr}}, \boldsymbol{q})$. Moreover, condition (2.5) entails the uniform convexity of the Helmholtz free energy

$$\Psi(\boldsymbol{\varepsilon}, \boldsymbol{e}^{\mathrm{tr}}, \boldsymbol{q}) = \sup_{\boldsymbol{\sigma}} \Big(\Phi(\boldsymbol{\sigma}, \boldsymbol{e}^{\mathrm{tr}}, \boldsymbol{q}) + \boldsymbol{\sigma} : \boldsymbol{\varepsilon} \Big)$$

with respect to the variables $(\boldsymbol{\varepsilon}, \boldsymbol{e}^{\mathrm{tr}}, \boldsymbol{q})$.

The stress-strain constitutive equation (2.1) is classically obtained from the free energy via the conjugacy relation

$$\boldsymbol{\varepsilon} = -\frac{\partial \Phi}{\partial \boldsymbol{\sigma}} = \mathbb{C}^{-1}\boldsymbol{\sigma} + \boldsymbol{e}^{\mathrm{tr}}.$$

The thermodynamic forces conjugated to the strain-like variables $\boldsymbol{e}^{\mathrm{tr}}$ and $\boldsymbol{q}$ are analogously

defined as

$$\boldsymbol{X} \in -\partial_{\boldsymbol{e}^{\mathrm{tr}}}\Phi = \boldsymbol{s} - \beta\partial\|\boldsymbol{e}^{\mathrm{tr}} - \boldsymbol{q}\| - h\boldsymbol{e}^{\mathrm{tr}} + A\boldsymbol{q} - \partial I_{\varepsilon_L}(\boldsymbol{e}^{\mathrm{tr}}), \tag{2.6a}$$

$$\boldsymbol{Q} \in -\partial_{\boldsymbol{q}}\Phi = \beta\partial\|\boldsymbol{e}^{\mathrm{tr}} - \boldsymbol{q}\| - H\boldsymbol{q} + A\boldsymbol{e}^{\mathrm{tr}}. \tag{2.6b}$$

This inclusions feature the occurrence of *subdifferentials* in the sense of convex analysis. Indeed, for all $\psi : X \to (-\infty, \infty]$ convex (possibly taking the value ∞ out of some convex constraining set) for some Hilbert space X (in particular $X = \mathbb{R}$, $\mathbb{R}^{3\times3}_{\mathrm{sym}}$, $(\mathbb{R}^{3\times3}_{\mathrm{sym}})^2$ etc.), the subdifferential $\partial\psi$ is defined for all $\boldsymbol{x} \in X$ such that $\psi(\boldsymbol{x}) < \infty$ as the (possibly empty) set

$$\partial\psi(\boldsymbol{x}) = \{\boldsymbol{y} \in X^*(\mathrm{dual}) \mid \boldsymbol{y} : (\boldsymbol{w} - \boldsymbol{x}) \leq \psi(\boldsymbol{w}) - \psi(\boldsymbol{x}) \ \forall \boldsymbol{w} \in X\}.$$

Note that if ψ is differentiable at $\boldsymbol{x}$ the subdifferential $\partial\psi(x)$ coincides with the usual gradient $\nabla\psi(\boldsymbol{x})$. The notion of subdifferential is particularly useful in non-smooth albeit convex situations, as that of the free energy $\Phi(\boldsymbol{\sigma}, \cdot, \cdot)$. Let us remark that we also use the notion of *partial subdifferential* without introducing new notation.

Relations (2.6) can be equivalently restated in the complementary form

$$\boldsymbol{X} = \boldsymbol{s} - \beta\frac{\boldsymbol{e}^{\mathrm{tr}} - \boldsymbol{q}}{\|\boldsymbol{e}^{\mathrm{tr}} - \boldsymbol{q}\|} - h\boldsymbol{e}^{\mathrm{tr}} + A\boldsymbol{q} - \gamma\frac{\boldsymbol{e}^{\mathrm{tr}}}{\|\boldsymbol{e}^{\mathrm{tr}}\|},$$
$$\boldsymbol{Q} = \beta\frac{\boldsymbol{e}^{\mathrm{tr}} - \boldsymbol{q}}{\|\boldsymbol{e}^{\mathrm{tr}} - \boldsymbol{q}\|} - H\boldsymbol{q} + A\boldsymbol{e}^{\mathrm{tr}}$$

where the scalar γ satisfies

$$\gamma \geq 0 \quad \text{and} \quad \gamma = 0 \quad \text{whenever} \quad \|\varepsilon^{\mathrm{tr}}\| < \varepsilon_L,$$

and we agree that $(\boldsymbol{e}^{\mathrm{tr}} - \boldsymbol{q})/\|\boldsymbol{e}^{\mathrm{tr}} - \boldsymbol{q}\|$ stands for an element of the unitary ball $\{\boldsymbol{y} \in \mathbb{R}^{3\times3}_{\mathrm{dev}} \mid \|\boldsymbol{y}\| \leq 1\}$ if $\boldsymbol{e}^{\mathrm{tr}} - \boldsymbol{q} = \boldsymbol{0}$.

2.3. Dissipation and constitutive relation

The dissipation (pseudo)potential is defined as the Fenchel-Legendre conjugate of the indicator function I_E of the *elastic domain*

$$E = \{(\boldsymbol{X}, \boldsymbol{Q}) \in (\mathbb{R}^{3\times3}_{\mathrm{dev}})^2 \mid F(\boldsymbol{X}, \boldsymbol{Q}) \leq 0\},$$

where F is the *yield function*

$$F(\boldsymbol{X},\boldsymbol{Q}) = \|\boldsymbol{X}\| + \kappa\|\boldsymbol{Q}\| - R.$$

Here, $R > 0$ is a material parameter corresponding to the *transformation radius* and $0 \leq \kappa < 1$ controls the activation of plastic effects. The dissipation potential is then given by duality as

$$D(\dot{\boldsymbol{e}}^{\mathrm{tr}},\dot{\boldsymbol{q}}) = \sup_{F(\boldsymbol{X},\boldsymbol{Q})\leq 0}\{\boldsymbol{X}:\dot{\boldsymbol{e}}^{\mathrm{tr}} + \boldsymbol{Q}:\dot{\boldsymbol{q}}\} = R\left(\kappa^{-1}\|\dot{\boldsymbol{q}}\| \vee \|\dot{\boldsymbol{e}}^{\mathrm{tr}}\|\right) \quad \text{for } \kappa > 0$$

and reduces to

$$D(\dot{\boldsymbol{e}}^{\mathrm{tr}},\dot{\boldsymbol{q}}) = R\|\dot{\boldsymbol{e}}^{\mathrm{tr}}\| + I_{\{\boldsymbol{0}\}}(\dot{\boldsymbol{q}}) \quad \text{for } \kappa = 0$$

where $I_{\{\boldsymbol{0}\}}$ is the indicator function of the singelton $\{\boldsymbol{0}\}$. The constitutive relation of the material can be expressed as

$$\partial_{(\dot{\boldsymbol{e}}^{\mathrm{tr}},\dot{\boldsymbol{q}})} D(\dot{\boldsymbol{e}}^{\mathrm{tr}},\dot{\boldsymbol{q}}) + \partial_{(\boldsymbol{e}^{\mathrm{tr}},\boldsymbol{q})}\Phi(\boldsymbol{\sigma},\boldsymbol{e}^{\mathrm{tr}},\boldsymbol{q}) \ni \boldsymbol{0} \tag{2.7}$$

which corresponds to a balance between *dissipative* ($\partial_{(\dot{\boldsymbol{e}}^{\mathrm{tr}},\dot{\boldsymbol{q}})} D(\dot{\boldsymbol{e}}^{\mathrm{tr}},\dot{\boldsymbol{q}})$) and *conservative* ($\partial_{(\boldsymbol{e}^{\mathrm{tr}},\boldsymbol{q})}\Phi(\boldsymbol{\sigma},\boldsymbol{e}^{\mathrm{tr}},\boldsymbol{q})$) actions. This evolution is equivalent to the constrained maximum problem

$$\text{maximize } \{\boldsymbol{X}:\dot{\boldsymbol{e}}^{\mathrm{tr}} + \boldsymbol{Q}:\dot{\boldsymbol{q}}\} \quad \text{subject to} \quad F(\boldsymbol{X},\boldsymbol{Q}) \leq 0$$

which corresponds to the *maximal dissipation* postulate. In particular, the latter can be equivalently expressed in complementarity form as

$$\dot{\boldsymbol{e}}^{\mathrm{tr}} = \zeta\frac{\boldsymbol{X}}{\|\boldsymbol{X}\|}, \qquad \dot{\boldsymbol{q}} = \kappa\zeta\frac{\boldsymbol{Q}}{\|\boldsymbol{Q}\|}, \qquad F \leq 0, \quad \zeta \geq 0, \quad \zeta F = 0. \tag{2.8}$$

In the limit case $\kappa = 0$, relations (2.8) ensure that the variable $\boldsymbol{q}$ does not evolve ($\dot{\boldsymbol{q}} = \boldsymbol{0}$) so that the model reduces to the standard Souza-Auricchio formulation without plasticization. This reduction argument has been made rigorous in [14] by means of the by-now classical *evolutionary* Γ*-convergence* approximation theory for energetic solutions of rate-independent systems from [26].

3. Analysis of the ARS model in one dimension

The aim of this section is to provide a detailed discussion of the ARS model in the uniaxial case. The interest in such an investigation is twofold. On the one hand, we complement the original analysis of [5] by illustrating the role of the different material parameters, discussing their effect on the evolution, and proposing an efficient fitting procedure from simple cyclic-traction experiments. These issues where largely not discussed in [5] and are of a clear relevance with respect to model validation. On the other hand, this analysis serves as a basis for the subsequent discussion of microstructure-dependence of materials parameters of Section 4, i.e. our novel modeling proposition.

Let σ and ε denote uniaxial stress and strain, respectively. The free energy in one dimension reads

$$\Phi(\sigma, \varepsilon^{\mathrm{tr}}, q) = -\frac{1}{2E}\sigma^2 - \sigma\varepsilon^{\mathrm{tr}} + \beta|\varepsilon^{\mathrm{tr}} - q| + \frac{h}{2}(\varepsilon^{\mathrm{tr}})^2 - A\varepsilon^{\mathrm{tr}}q + \frac{H}{2}q^2 + I_{\varepsilon_L}(\varepsilon^{\mathrm{tr}}),$$

(where now I_{ε_L} is the indicator function of the interval $[-\varepsilon_L, \varepsilon_L]$) yielding the stress-strain constitutive relation

$$\varepsilon = -\frac{\partial\Phi}{\partial\sigma} = \frac{\sigma}{E} + \varepsilon^{\mathrm{tr}}$$

and the thermodynamic forces

$$X = \sigma - \tilde{\beta} - h\varepsilon^{\mathrm{tr}} + Aq - \gamma \in -\partial_{\varepsilon^{\mathrm{tr}}}\Phi, \tag{3.1}$$

$$Q = \tilde{\beta} - Hq + A\varepsilon^{\mathrm{tr}} \in -\partial_q\Phi \tag{3.2}$$

The values γ and $\tilde{\beta}$ above are selection of the corresponding subdifferentials. In particular,

$$\tilde{\beta} \in \beta\frac{\varepsilon^{\mathrm{tr}} - q}{|\varepsilon^{\mathrm{tr}} - q|} = \begin{cases} \beta(\varepsilon^{\mathrm{tr}} - q)/|\varepsilon^{\mathrm{tr}} - q| & \text{for } \varepsilon^{\mathrm{tr}} \neq q \\ [-\beta, \beta] & \text{for } \varepsilon^{\mathrm{tr}} = q \end{cases} \tag{3.3}$$

and

$$\gamma \in \partial I_{\varepsilon_L}(\varepsilon^{\mathrm{tr}}).$$

Finally, the yield function reads

$$F = |X| + \kappa|Q| - R,$$

so that the flow rule is

$$\dot{\varepsilon^{\rm tr}} = \zeta \frac{\partial F}{\partial X} = \zeta \frac{X}{|X|}, \quad \dot{q} = \zeta \frac{\partial F}{\partial Q} = \kappa \zeta \frac{Q}{|Q|}, \quad \zeta \geq 0, \quad F \leq 0, \quad \zeta F = 0. \tag{3.4}$$

In order to analyze the behavior of the model, we argue on trajectories in the $(\varepsilon^{\rm tr}, q)$-plane. Note that the sign of X is driven by the stress σ, whereas the sign of Q depends only on the internal variables $(\varepsilon^{\rm tr}, q)$. It is hence useful to identify the regions of the $(\varepsilon^{\rm tr}, q)$-plane which correspond to positive or negative values of Q. We shall concentrate from the very beginning on the case $0 \leq q \leq \varepsilon^{\rm tr}$ (implying $\varepsilon^{\rm m} \geq 0$),corresponding indeed to tension experiments. From relation (3.2) we get that

$$Q \geq 0 \iff q \leq q_*(\varepsilon^{\rm tr}) := \frac{A}{H}\varepsilon^{\rm tr} + \frac{\beta}{H}.$$

The situation is illustrated in Figure 2, referring to the case of practical interest $q_*(\varepsilon_L) \leq \varepsilon_L$.

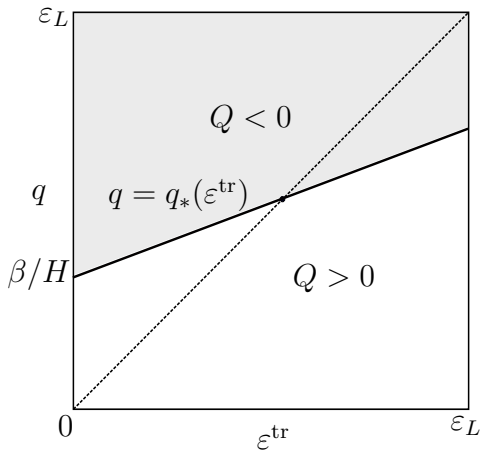

Figure 2: The thermodynamic force Q changes sign across the line $q = q_*(\varepsilon^{\rm tr})$.

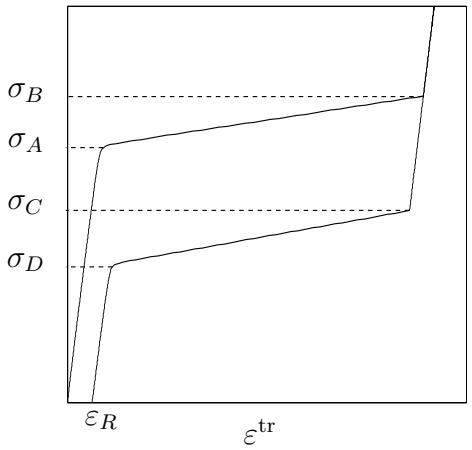

Figure 3: Threshold stresses and residual strain for a loading-unloading cycle.

Let us introduce the threshold stresses σ_A (martensite-start threshold), σ_B (martensite-finish), σ_C (austenite-start), σ_D (austenite-finish) and the residual strain ε_R as illustrated in Figure 3. As these quantities change during the successive cycles, we indicate the successive cycles with additional indexes and the limit cycle by the index ∞.

3.1. Martensite-start stress σ_A

Starting from the initial conditions $\varepsilon_0^{\rm tr} = q_0 =: \varepsilon_0 \geq 0$ at zero stress (note that $\varepsilon^{\rm tr} = q$ for, $\sigma = 0$, as results from the analysis of the unloading phase, Subsection 3.5), the activation condition upon loading

$$|\sigma_A - \tilde{\beta} + (A-h)\varepsilon_0| + \kappa|\tilde{\beta} + (A-H)\varepsilon_0| = R$$

holds for $\tilde{\beta} = \beta$ and $\sigma_A - \beta + (A-h)\varepsilon_0 > 0$. In particular, at activation one has that

$$\sigma_A = R + \beta + (h-A)\varepsilon_0 - \kappa|\beta + (A-H)\varepsilon_0| \tag{3.5}$$

Namely, the activation stress σ_{A0} in the first loading cycle (that is for $\varepsilon_0 = 0$) is given by

$$\sigma_{A0} = R + (1-\kappa)\beta.$$

3.2. Loading phase

We shall consider now the activated loading case $\dot{\sigma} > 0$ and $\dot{\varepsilon}^{\rm tr} = \zeta > 0$. If $Q(0) \geq 0$ then $Q \geq 0$ during the whole loading phase (see Figure 5, trajectories a_1 and a_2). In fact, we have that

$$Q < 0 \implies \dot{q} \leq 0 \implies \dot{Q} = A\dot{\varepsilon}^{\rm tr} - H\dot{q} \geq 0.$$

Since $X(t) \geq 0$ in the activated loading phase, we have

$$F(t) = X(t) + \kappa Q(t) - R \equiv 0$$

Let us concentrate here on the case $Q > 0$ and discuss the situation $Q = 0$ in Subsection 3.3 below. If $Q > 0$ then $\dot{q} = \kappa\zeta = \kappa\dot{\varepsilon}^{\rm tr}$ and

$$0 = \dot{F} = \dot{\sigma} + (2\kappa A - h - \kappa^2 H)\dot{\varepsilon}^{\rm tr}. \tag{3.6}$$

Relation (3.6) entails in particular that by assuming

$$h + \kappa^2 H > 2\kappa A,$$

$\dot\sigma$ and $\dot\varepsilon^{\rm tr}$ have the same sign, see Subsection 3.4. We hence refer to this condition as the *nonsoftening* constraint.

The material parameters have indeed to fulfill the further constraint

$$\kappa\beta \le R \tag{3.7}$$

which we refer to as the *continuity constraint* as it turns out to be necessary for the continuity of the evolution. In order to see this, consider a loading process starting from $q_0 = \varepsilon_0^{\rm tr} = 0$ with $Q_0 = \tilde\beta$ for some $\beta \in [-\beta, \beta]$. After activation we have that $\varepsilon^{\rm tr} - q > 0$, so that $\tilde\beta = \beta$. If $\varepsilon^{\rm tr} = 0^+$ and $q = 0^+$ in a right neighborhood of the activation time one necessarily has that $0 = F \ge \kappa\beta - R$, that is (3.7) . Let us mention that condition (3.7) appears to be little restrictive with respect to applications, as β and R are comparable in size, whereas (see Section 4) κ is typically few percentage points.

3.3. The case $Q \equiv 0$

In the parameter range $A \le \kappa H$ it is possible to have $Q \equiv 0$ during the loading process. In fact, by letting $\dot Q = 0$, hence $\dot q = (A/H)\dot\varepsilon^{\rm tr}$, one has that the flow rule (3.4) is satisfied. The consistency condition $\dot F = 0$ then yields

$$0 = \dot F = \dot\sigma - (A^2/H - h)\dot\varepsilon^{\rm tr},$$

to be compared with (3.6) for the case $Q > 0$. This entails in particular that the slope $d\sigma/d\varepsilon^{\rm tr}$ changes when Q vanishes:

$$\frac{d\sigma}{d\varepsilon^{\rm tr}} = \begin{cases} h + \kappa^2 H - 2\kappa A & \text{if } Q > 0, \\ h - A^2/H & \text{if } Q = 0. \end{cases}$$

Note that both slopes are positive due to the convexity condition (2.5). During the first loading cycle, condition $Q > 0$ holds during the whole loading phase iff

$$\kappa\varepsilon_L \le q_*(\varepsilon_L).$$

Otherwise, the slope $d\sigma/d\varepsilon^{\rm tr}$ changes during loading, see Figure. 4. This effect was originally not observed in [5].

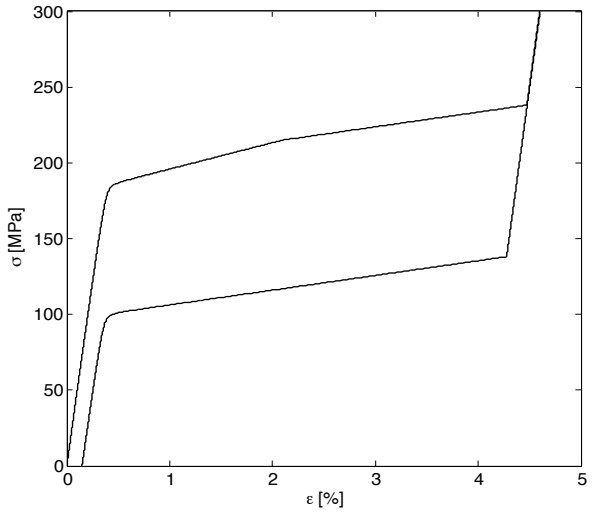

Figure 4: Loading-unloading cycle for $\varepsilon_L = 4\%$, $\beta = 150$ MPa, $R = 50$ MPa, $\kappa = 0.1$, $H = 10^5$ MPa, $h = A = 10^3$ MPa. In particular, one has that $\kappa\varepsilon_L = 4 \cdot 10^{-3} > q_*(\varepsilon^{\mathrm{tr}}) = 1.9 \cdot 10^{-3}$. The hardening curve exhibits a change in slope under loading.

3.4. Saturation ($\varepsilon^{\mathrm{tr}} = \varepsilon_L$)

Define $Q_0 = \beta + (A - H)\varepsilon_0$ to be the value of Q at the beginning of a the loading cycle (i.e. at zero stress). As $\varepsilon^{\mathrm{tr}}$ obviously saturates at ε_L, we are left with analyzing the saturation value q_L for q. In Figure 5 the trajectories $t \mapsto (\varepsilon^{\mathrm{tr}}(t), q(t))$ for different starting points $\varepsilon_0^{\mathrm{tr}} = q_0 =: \varepsilon_0$ are illustrated. The trajectories depend on the initial value Q_0 and the relative size of κ and A/H. Let us divide the explanation in the two cases $Q_0 \geq 0$ (corresponding to trajectories a) and $Q_0 < 0$ (trajectories b, respectively) in Figure 5.

- Let $Q_0 \geq 0$. In case $Q(t) > 0$ during the whole loading process (i.e. for any $t < t_L$, t_L being the saturation time), then $\dot{q} = \kappa\dot{\varepsilon}^{\mathrm{tr}}$, so that the limit q_L is given by

$$q_L = \varepsilon_0 + \kappa(\varepsilon_L - \varepsilon_0).$$

  This corresponds to trajectory a_1 in Figure 5. Otherwise, if $Q(t)$ vanishes at some

$t_0 < t_L$, then the limit q_L is obtained as follows

$$Q_L := Q(t_L) = \beta - Hq_L + A\varepsilon_L = 0 \quad \Longrightarrow \quad q_L = q_*(\varepsilon_L).$$

This is trajectory a_2 in Fig. 5). We can summarize these two cases with the formula

$$q_L = (\varepsilon_0 + \kappa(\varepsilon_L - \varepsilon_0)) \wedge q_*(\varepsilon_L).$$

In particular, the saturation value q_{L0} at the first cycle ($\varepsilon_0 = 0$) is

$$q_{L0} = \kappa\varepsilon_L \wedge q_*(\varepsilon_L).$$

- Let $Q_0 < 0$. The trajectory $t \mapsto (\varepsilon^{\rm tr}(t), q(t))$ descends with slope κ until it crosses the line $q = q_*(\varepsilon)$. If the trajectory crosses this line at $\varepsilon = \varepsilon_* < \varepsilon_L$, then it starts rising with slope $\kappa \wedge A/H$, so that

$$q_L = (q_*(\varepsilon_*) + \kappa(\varepsilon_L - \varepsilon_*)) \wedge q_*(\varepsilon_L).$$

The intersection point $(\varepsilon_*, q_*(\varepsilon_*))$ is obtained as

$$\varepsilon_0 - \kappa(\varepsilon_* - \varepsilon_0) = q_*(\varepsilon_*) \quad \Longrightarrow \quad \varepsilon_* = \frac{\varepsilon_0(1+\kappa) - \beta/H}{A/H + \kappa}.$$

These corresponds to the trajectories b_1 (for $\kappa \geq A/H$) and b_2 ($\kappa < A/H$, respectively) in Figure 5. If $(\varepsilon^{\rm tr}(t), q(t)$ never crosses $q = q_*(\varepsilon)$, then $q_L = \varepsilon_0 - \kappa(\varepsilon_L - \varepsilon_0)$ (trajectory b_3 in Figure 5). This case is less relevant, as it is not reachable under cyclic loading starting from $\varepsilon_0^{\rm tr} = 0$ (see Figure 7).

Since in all cases of practical interest one has $X_L := X(t_L) \geq 0$ and $Q_L \geq 0$, the saturation stress σ_B is obtained from the condition $X_L + \kappa Q_L = R$ as

$$\sigma_B = R + \beta(1-\kappa) + (h - \kappa A)\varepsilon_L - (A - \kappa H)q_L.$$

In particular, starting from $\varepsilon_0 = 0$ one has

$$\sigma_{B0} = R + \beta(1-\kappa) + (h - \kappa A)\varepsilon_L + (\kappa H - A)\left(\kappa\varepsilon_L \wedge q_*(\varepsilon_L)\right).$$

The value of σ_B changes during the different loading cycles as an effect of the change of q_L. In particular, one has that

$$\Delta\sigma_B = (\kappa H - A)\Delta q_L.$$

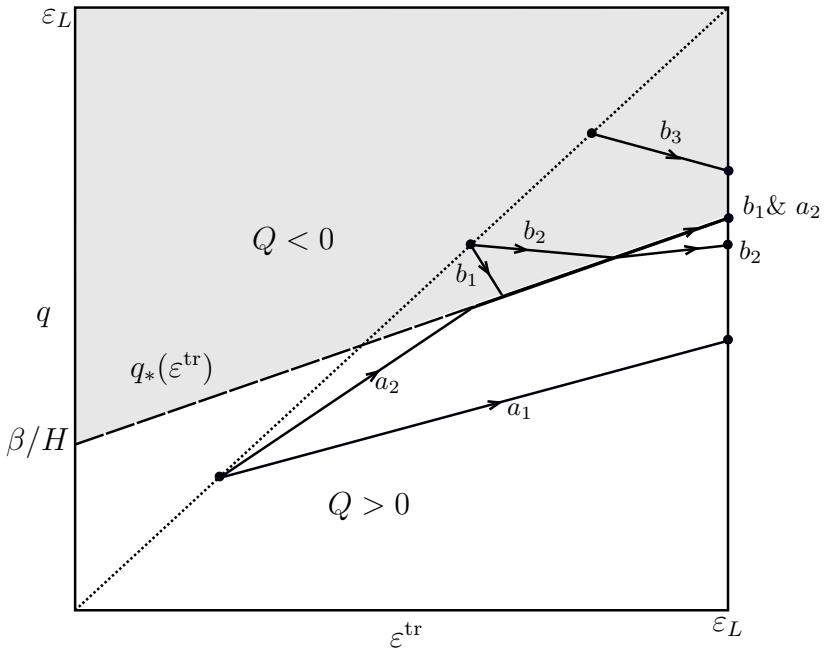

Figure 5: Saturation value of q for different starting points $\varepsilon_0 = q_0$ and different values of κ (greater than A/H in cases a_2 and b_1, smaller than A/H in case b_2).

3.5. Unloading phase

At saturation we have $X = X_L \geq 0$, $Q = Q_L \geq 0$ and $X_L + \kappa Q_L = R$. Upon unloading from saturation the strains q and $\varepsilon^{\rm tr}$ remain constant until transformation starts. As Q does not depend on σ, the threshold stress σ_C can be computed as

$$\sigma_C - \beta - h\varepsilon_L + Aq_L = -(\sigma_B - \beta - h\varepsilon_L + Aq_L).$$

By using the already obtained expression of σ_B we have that

$$\sigma_C = 2\beta - \sigma_{A0} + (h + \kappa H)\varepsilon_L - (\kappa H + A)q_L.$$

The change in σ_C during the successive cycles is

$$\Delta\sigma_C = -(\kappa H + A)\Delta q_L.$$

The threshold stresses are usually observed to decrease in successive cycles, i.e., $\Delta\sigma_B < 0$ and $\Delta\sigma_C < 0$. This corresponds to the following relations

$$(\kappa H - A)\Delta q_L < 0, \quad -(\kappa H + A)\Delta q_L < 0.$$

In order to ensure the above mentioned progressive degradation of the mechanical response of the material under cyclic loading we may hence assume

$$A > \kappa H. \tag{3.8}$$

We refer to the latter as the *degradation condition* in the following.

3.6. First residual strain ε_{R0}

We now investigate the residual strain after the first cycle, i.e starting from the initial state $\varepsilon_0^{\rm tr} = q_0 = 0$. All possible trajectories in the $(\varepsilon^{\rm tr}, q)$-plane are plotted in Figure 6. Strain recovery ends at $\varepsilon^{\rm tr} = q$. At that point, the final value of X belongs to the set

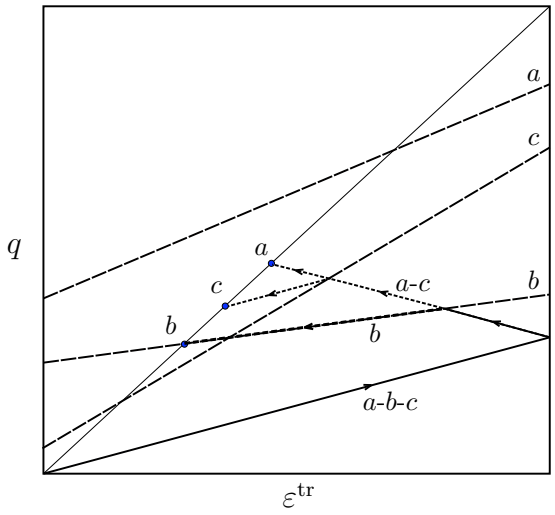

Figure 6: First cycle residual strain. For fixed κ, the possible end points a, b and c, after a complete loading-unloading cycle starting from $q = \varepsilon^{\rm tr} = 0$ (dotted lines), are shown for three different choices of $q_*(\varepsilon^{\rm tr})$ (dashed lines).

$\sigma - h\varepsilon^{\rm tr} + Aq + [-\beta, \beta]$. We distinguish three cases:

a) $Q > 0$ in the whole loading and unloading phase. Then $\dot{q} = \kappa|\dot{\varepsilon}^{\rm tr}|$ and the residual strain is

$$\varepsilon_{R0} = \frac{2\kappa}{1+\kappa}\varepsilon_L.$$

This particularly simple case follows when $\varepsilon_{R0} \leq q_*(\varepsilon_{R0})$, that is when

$$\frac{2\kappa}{1+\kappa}\,(H - A) \leq \frac{\beta}{\varepsilon_L}. \tag{3.9}$$

We shall refer specifically to condition (3.9) for the fitting of the materials parameters in Subsection 3.12 below.

b) $Q \leq 0$ during the unloading phase and the degradation condition (3.8) holds, i.e.,

$$\frac{2\kappa}{1+\kappa}\,(H - A) \geq \frac{\beta}{\varepsilon_L} \quad \text{and} \quad \kappa > \frac{A}{H}.$$

Then, the residual strain ε_{R0} can be computed as the intersection of the line $q = q_*(\varepsilon^{\rm tr})$ with the diagonal, namely

$$\varepsilon_{R0} = \frac{\beta}{H - A}.$$

c) $Q \leq 0$ during the unloading phase and the degradation condition (3.8) does not hold, i.e.,

$$\frac{2\kappa}{1+\kappa}\,(H - A) \geq \frac{\beta}{\varepsilon_L} \quad \text{and} \quad \kappa < \frac{A}{H}.$$

Then, one has that

$$\varepsilon_{R0} = \frac{2\kappa}{1-\kappa}\frac{\beta + (A - \kappa H)\varepsilon_L}{A + \kappa H}.$$

It is easily seen that all three cases above can be summarized by

$$\varepsilon_{R0} = \frac{2\kappa}{1-\kappa}\frac{\beta + (A - \kappa H)\varepsilon_L}{A + \kappa H} \wedge \frac{\beta}{H - A} \wedge \frac{2\kappa}{1+\kappa}\varepsilon_L.$$

The activation stress σ_{A1} after the first cycle, with residual strain ε_{R0}, is

$$\sigma_{A1} = R + \beta + (h - A)\varepsilon_R - \kappa|\beta + (A - H)\varepsilon_{R0}|.$$

In case a), where $Q > 0$,

$$\sigma_{A1} = \sigma_{A0} + \varepsilon_{R0}[h - \kappa A - (A - \kappa H)]. \tag{3.10}$$

Let us comment that in order to have $\sigma_{A1} \leq \sigma_{A0}$ it is necessary that

$$(1 + \kappa)A \geq h + \kappa H.$$

The latter is in the same spirit of (3.8), although not equivalent.

3.7. Limit residual strain $\varepsilon_{R\infty}$

We shall now discuss the behavior of the limit strain residual strain $\varepsilon_{R\infty} = \lim \varepsilon_{Rk}$.

If the degradation condition (3.8) does not hold and $Q(0) \geq 0$, then $Q \geq 0$ for all times. In fact,

$$\dot{Q} = H\left(\frac{A}{H}\dot{\varepsilon}^{\rm tr} - \dot{q}\right)$$

and $|\dot{q}| = \kappa|\dot{\varepsilon}^{\rm tr}|$. Then, q is always increasing and does not cross the line $q = q_*(\varepsilon^{\rm tr})$. The saturation value of $\varepsilon^{\rm tr}$ is obtained from the intersection of the line $q = q_*(\varepsilon^{\rm tr})$ and the diagonal $q = \varepsilon^{\rm tr}$ in case such an intersection point exists with $\varepsilon^{\rm tr} < \varepsilon_L$. Otherwise one has $\varepsilon_{R\infty} = \varepsilon_L$. Namely,

$$\kappa \geq A/H \Longrightarrow \varepsilon_{R\infty} = \frac{\beta}{H - A} \wedge \varepsilon_L.$$

The limit value of q_L is simply

$$q_{L\infty} = q_*(\varepsilon_{R\infty}).$$

Assume now that the degradation condition (3.8) holds. The typical situation is represented in Figure 7. In order to be cycle-invariant, the limit cycle has to be a parallelogram. One of its diagonals belongs to the line $q = q_*(\varepsilon^{\rm tr})$. The other two vertices are on the diagonal $q = \varepsilon^{\rm tr}$ and on the limit line $\varepsilon^{\rm tr} = \varepsilon_L$, respectively. The sides of the parallelogram are $q-$descending above the line $q_*(\varepsilon^{\rm tr})$ and ascending below. These conditions uniquely identify the parallelogram. One obtains the limit value $\varepsilon_{R\infty}$ (which correspond to the abscissa of the left corner of the limit parallelogram) as

$$\varepsilon_{R\infty} = \frac{2A\beta + (A^2 - \kappa^2 H^2)\varepsilon_L}{2AH - (A^2 + \kappa^2 H^2)} \wedge \varepsilon_L.$$

The ordinate of the left corner gives $q_{L\infty}$, namely

$$q_{L\infty} = \varepsilon_{R\infty} + \frac{\kappa^2 H}{A}(\varepsilon_L - \varepsilon_{R\infty}).$$

We can summarize the above discussion the following formula comprehensive of both cases

$$\varepsilon_{R\infty} = \frac{2A\beta + (A^2 - \kappa^2 H^2)^+ \varepsilon_L}{2A(H - A) + (A^2 - \kappa^2 H^2)^+} \wedge \varepsilon_L. \tag{3.11}$$

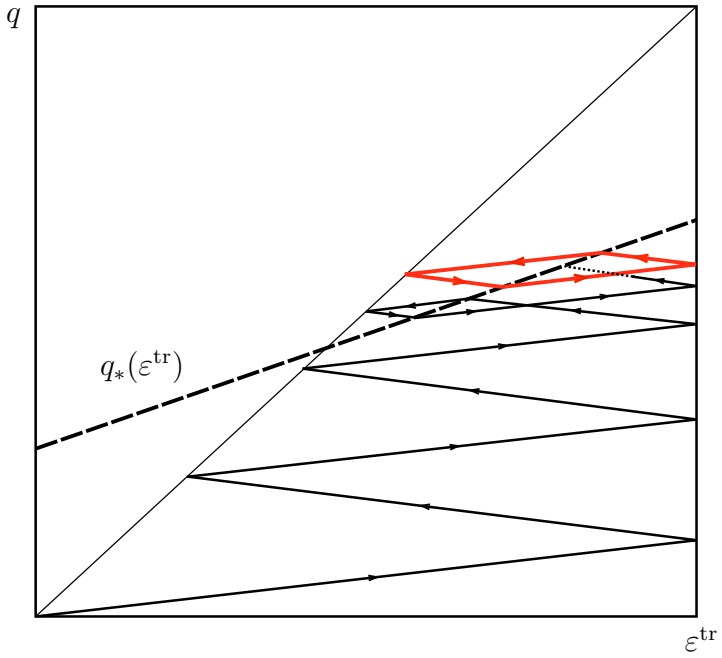

Figure 7: Limit cycle for $k < A/H$

3.8. Summary

As already commented, the above analysis allows us to express the relevant physical quantities obtained from the experimental data in terms of material parameters. We

summarize these findings in the following list of relations

$$\sigma_{A0} = R + \beta(1-\kappa), \tag{3.12a}$$

$$q_{L0} = \kappa\varepsilon_L \wedge (\beta + A\varepsilon_L)/H, \tag{3.12b}$$

$$\sigma_{B0} - \sigma_{A0} = (h - \kappa A)\varepsilon_L + (\kappa H - A)q_{L0}, \tag{3.12c}$$

$$\sigma_{A\infty} - \sigma_{A0} = 2\kappa\beta + \varepsilon_{R\infty}((h + \kappa A) - (A + \kappa H)), \tag{3.12d}$$

$$\sigma_{B0} + \sigma_{C0} = 2\left(\beta + h\varepsilon_L - Aq_{L0}\right), \tag{3.12e}$$

$$\sigma_{A1} - \sigma_{A0} = \varepsilon_R(h - \kappa A - (A - \kappa H)), \tag{3.12f}$$

$$\Delta\sigma_B = -(A - \kappa H)\Delta q_L, \tag{3.12g}$$

$$\Delta\sigma_C = -(A + \kappa H)\Delta q_L, \tag{3.12h}$$

$$\varepsilon_{R0} = \frac{2\kappa}{1-\kappa}\frac{\beta + (A - \kappa H)\varepsilon_L}{A + \kappa H} \wedge \frac{\beta}{H - A} \wedge \frac{2\kappa}{1+\kappa}\varepsilon_L, \tag{3.12i}$$

$$\varepsilon_{R\infty} = \frac{2A\beta + (A^2 - \kappa^2 H^2)^+\varepsilon_L}{2A(H - A) + (A^2 - \kappa^2 H^2)^+} \wedge \varepsilon_L. \tag{3.12j}$$

Note that relation (3.12d) follows from (3.5) by observing that $Q \leq 0$ at the beginning of the limit cycle.

3.9. Constraints on the parameters

The above discussion lead to the introduction of constraints on the possible choice of material parameters. For the reader's convenience we summarize them here

$$\text{Convexity:} \quad hH > A^2 \tag{3.13a}$$

$$\text{Nonsoftening:} \quad h + \kappa^2 H > 2\kappa A \tag{3.13b}$$

$$\text{Continuity:} \quad \kappa\beta \leq R \tag{3.13c}$$

These conditions are assumed throughout the analysis. Additionally, we have identified condition

$$\text{Degradation:} \quad A \geq \kappa H \tag{3.14}$$

which entails mechanical degradation and condition

$$\frac{2\kappa}{1+\kappa}\,(H-A) \le \frac{\beta}{\varepsilon_L} \tag{3.15}$$

under which we develop the fitting procedure in Subsection 3.12. Let us mention that all these conditions appear to be compatible with experiments [11, 12], see Section 4.

3.10. Limit case $\kappa \to 0$

In the limit $\kappa \to 0$, we formally have $q_{L0} = 0$ and

$$\sigma_{A0} = R_0 + \beta_0, \qquad \sigma_{B0} - \sigma_{A0} = h_0\varepsilon_L, \tag{3.16a}$$

$$\sigma_{A\infty} - \sigma_{A0} = \varepsilon_{R\infty}(h_0 - A_0), \qquad \varepsilon_{R0} = 0, \tag{3.16b}$$

$$\frac{\sigma_{A0} + \sigma_{C0}}{2} = \beta_0 + \varepsilon_L\frac{h_0}{2}, \qquad \varepsilon_{R\infty} = \frac{\beta_0 + \varepsilon_L A_0/2}{H_0 - A_0/2}. \tag{3.16c}$$

The latter correspond to the original Souza-Auricchio model [32], except for the occurrence of the value $\varepsilon_{R\infty} > 0$ (note however that in this limiting case saturation is obtained after an infinite number of cycles only). By inverting (3.16), one can obtain the free-energy parameters

$$\beta_0 = \sigma_{A0} - \frac{\sigma_{B0} - \sigma_{C0}}{2}, \quad h_0 = \frac{\sigma_{B0} - \sigma_{A0}}{\varepsilon_L}, \quad A_0 = h_0 + \frac{\sigma_{A\infty} - \sigma_{A0}}{\varepsilon_{R\infty}},$$

$$R_0 = \sigma_{A0} - \beta_0, \quad H_0 = \frac{\beta_0}{\varepsilon_{R\infty}} + (1+\lambda)A_0$$

where we have used he short-hand notation $\lambda = (\varepsilon_L - \varepsilon_{R\infty})/(2\varepsilon_{R\infty})$. These expressions turn out to be useful in order to evaluate the size of the free-energy parameters as a function of the empirically measurable threshold stresses and remanent strain for small κ. At the same time, they allow to check the fulfillment of the convexity constraint $h_0H_0 - A_0^2 > 0$. In general, for increasing values of $\sigma_{A\infty} - \sigma_{A0}$, the minimum value of h_0 ensuring convexity increases as well. This corresponds to the hardening case $(\sigma_{B0} - \sigma_{A0})/\varepsilon_L > 0$. A first order approximation with respect to κ is easily obtained. By letting

$$h = h_0 + \kappa h_1, \quad \beta = \beta_0 + \kappa\beta_1, \quad A = A_0 + \kappa A_1, \qquad H = H_0 + \kappa H_1,$$

one gets

$$h_1 = 2A_0 + \mathrm{O}(\kappa), \qquad A_1 = \frac{\beta_0}{\varepsilon_{R\infty}} + (2-\lambda)A_0 + \mathrm{O}(\kappa),$$
$$\beta_1 = -\varepsilon_L A_0 + \mathrm{O}(\kappa), \qquad H_1 = \frac{\beta_1}{\varepsilon_{R\infty}} + (1+\lambda)A_1 + \mathrm{O}(\kappa).$$

3.11. The case $A = 0$.

In this case we have that

$$\varepsilon_{R0} = \frac{\beta}{H} \wedge \frac{2\kappa}{1+\kappa}\varepsilon_L, \qquad \varepsilon_{R\infty} = \frac{\beta}{H} \wedge \varepsilon_L.$$

Hence, by assuming $\varepsilon_L > \varepsilon_{R\infty} > \varepsilon_R$, we obtain $\beta/H = \varepsilon_{R\infty}$. In particular, we can explicitly deduce the materials parameters in terms of observable quantities as follows

$$\kappa = \frac{\varepsilon_{R0}}{2\varepsilon_L - \varepsilon_{R0}}, \qquad h + \kappa H = \frac{\sigma_{A\infty} - \sigma_{A0}}{\varepsilon_{R\infty}}, \quad h + \kappa^2 H = \frac{\sigma_{B0} - \sigma_{A0}}{\varepsilon_L}$$

$$\beta = \varepsilon_{R\infty} H, \qquad R = \sigma_{A0} - \beta(1-\kappa).$$

3.12. The general case $\kappa \neq 0$ and $A \neq 0$.

Beside the elastic parameters and the empirically measurable ε_L, all material parameters $(R, \beta, \kappa, h, H, A)$ have to be fitted with respect to experiments. We present here a procedure in order to determine them in terms of experimentally the observable quantities

$$(\varepsilon_L, \sigma_{A0}, \sigma_{B0}, \sigma_{C0}, \sigma_{A\infty}, \varepsilon_{R0}, \varepsilon_{R\infty}).$$

Parameter R can be obtained in terms of σ_{A0}, κ, and β as

$$R = \sigma_{A0} - (1-\kappa)\beta. \tag{3.17}$$

For the sake of simplicity, we shall present here a fitting procedure under the additional assumption (3.15) as this greatly reduces technicalities being at the same time well-adapted to experimental situations. By using this condition we have that (see Subsection 3.7) $\varepsilon_{R0} = 2\kappa\varepsilon_L/(1+\kappa)$ which immediately entails

$$\kappa = \frac{\varepsilon_{R0}}{2\varepsilon_L - \varepsilon_{R0}}. \tag{3.18}$$

Moreover, we also have that $q_{L0} = \kappa\varepsilon_L$, so the parameter q_{L0} can be explicitly written in terms of measurable quantities. Note that condition (3.15) leads to the case a of Figure 6. In particular, the limit cycle is not reached at the first few cycles (see Figure 7).

Four conditions are needed in order to determine the parameters β, h, A, and H. By combining equations (3.12c) and (3.12e), with $q_{L0} = \kappa\varepsilon_L$, we may impose

$$2\beta + \varepsilon_L(h - \kappa^2 H) = \sigma_{A0} + \sigma_{C0} \tag{3.19}$$

which calls for both the activation and the deactivation stresses σ_{A0} and σ_{C0} at the first loading cycle. Secondly, we impose condition (3.12d)

$$2\kappa\beta + \varepsilon_{R\infty}(h - (1-\kappa)A - \kappa H) = \sigma_{A\infty} - \sigma_{A0} \tag{3.20}$$

which takes directly into account the decreasing of the activation stress, a distinctive fatigue effect. Third, equation (3.12j) for $\varepsilon_{R\infty}$ gives

$$(\varepsilon_L + \varepsilon_{R\infty})A^2 - 2(\varepsilon_{R\infty}H - \beta)A - \kappa^2(\varepsilon_L - \varepsilon_{R\infty})H^2 = 0. \tag{3.21}$$

This condition features the saturation residual strain, one of the most important value to be incorporated in the model. A fourth equation being needed, one can for instance resort on that ruling the slope of the activated loading line, namely

$$(h - \kappa A) - \kappa(A - \kappa H) = (\sigma_{B0} - \sigma_{A0})/\varepsilon_L. \tag{3.22}$$

The parameters β, h, A, and H are then obtained by solving the systems (3.19)-(3.22) and by checking that indeed these solutions fulfill (3.13) as well as (3.15). Among the conditions (3.13), for realistic experimental data, only the condition (3.13a) is sometimes disobeyed. In this case, the procedure we have followed is to impose the condition $hH - A^2 = C$ with $C > 0$ as small as possible (while retaining the stability of the algorithm) and to remove from the system one of the equations (3.19)-(3.22), in particular (3.20). Finally, R is obtained from the formerly calculated parameters κ, β through (3.17).

4. Microstructure-dependent model extension

As mentioned in the Introduction, the polycrystalline microstructure of the SMA specimen has been proved to affect the emergence of the pseudoelastic behavior and the occurrence of fatigue [30]. The experimental investigations in [9, 10, 11, 12] clearly indicate the proportion of recrystallized material and the mean crystal-grain size as relevant quantities in connection with the functional properties of the material. The proportion of crystallized material is particularly relevant in connection with cold-worked specimens, where the material is usually a mixture of austenite, martensite and amorphous phase due to the severe plastic deformations of the working process. The material recrystallizes due to heat treatment. As soon as the material is fully recrystallized the relevant microstructural feature turns out to be the mean crystal-grain size [37]. Indeed, heat treatment favors crystal-grain coarsening that is the growth of the mean crystal-grains radius. More refined descriptions would include the size distribution of the grains and their texture of crystallographic orientation [17].

Our aim is that of proposing a phenomenological model of the isothermal mechanical behavior of SMAs taking into account the different functional regimes as presented in [9, 11]. To this end we include the crystalized proportion $\phi \in [0, 1]$ and the mean crystal-grain size $r > 0$ as additional parameters in the model. In particular, we extend the ARS model (see Section 2) by letting the material parameters depend additionally on ϕ and r. The focus will be on choosing such microstructure-dependence of the parameters in order to fit the experimental evidence from [9, 11]. The result of such a fitting is illustrated in Figure 9 where experiments (left) and numerical simulation (right) are compared.

4.1. Crystallized proportion dependence

The mechanical response of the amorphous phase $\phi = 0$ can be assumed to be elastic. We proceed by simply letting the inelastic behavior of the material scale linearly with the crystallized proportion ϕ. By denoting by $\bar{\varepsilon}^{\mathrm{tr}}$ the transformation strain of the fully-crystallized material, we assume that the transformation strain $\varepsilon^{\mathrm{tr}}$ of the ϕ-crystallized

specimen satisfies

$$\varepsilon^{\mathrm{tr}} = \phi\overline{\varepsilon}^{\mathrm{tr}}.$$

This corresponds to consider the material as a simple *mixture* of an elastic and an inelastic component. In particular, by denoting by Φ_{inel} the inelastic part to the free energy

$$\Phi_{\mathrm{inel}}(\boldsymbol{\sigma}, \boldsymbol{e}^{\mathrm{tr}}, \boldsymbol{q}) := \Phi(\boldsymbol{\sigma}, \boldsymbol{e}^{\mathrm{tr}}, \boldsymbol{q}) + \frac{1}{2}\boldsymbol{\sigma} : \mathbb{C}^{-1}\boldsymbol{\sigma}.$$

We are indeed assuming that the free energy of the ϕ-crystallized body takes the form

$$\Phi(\boldsymbol{\sigma}, \boldsymbol{e}^{\mathrm{tr}}, \boldsymbol{q}; \phi) = -\frac{1}{2}\boldsymbol{\sigma} : \mathbb{C}^{-1}\boldsymbol{\sigma} + \phi\Phi_{\mathrm{inel}}(\boldsymbol{\sigma}, \boldsymbol{e}^{\mathrm{tr}}, \boldsymbol{q}). \tag{4.1}$$

By working out the explicit dependence of Φ_{inel} on these parameters from (2.4), we obtain that

$$\phi\Phi_{\mathrm{inel}}(\boldsymbol{\sigma}, \boldsymbol{e}^{\mathrm{tr}}, \boldsymbol{q}; \beta, H, A, h, \varepsilon_L) = \Phi_{\mathrm{inel}}\left(\boldsymbol{\sigma}, \phi\boldsymbol{e}^{\mathrm{tr}}, \phi\boldsymbol{q}; \beta, \phi^{-1}H, \phi^{-1}A, \phi^{-1}h, \phi\varepsilon_L\right).$$

Then, position (4.1) is equivalent to assuming the following scalings on ϕ for the material parameters

$$\beta(\phi) = \overline{\beta}, \quad H(\phi) = \phi^{-1}\overline{H}, \quad A(\phi) = \phi^{-1}\overline{A}; \quad h(\phi) = \phi^{-1}\overline{h}, \quad \varepsilon_L(\phi) = \phi\overline{\varepsilon}_L$$

where, again, bars correspond to the fully-crystallized situation. Note that the case $\phi = 0$ will be amenable as well due to a cancellation in the energy, see (4.2) below. By following the same linear scaling assumption for the dissipation potential we impose $D(\phi) = \phi\overline{D}$, which corresponds to

$$\kappa(\phi) = \overline{\kappa}, \qquad R(\phi) = \phi\overline{R}.$$

Let us now consider the above scaling assumptions in light of the limit formulas (3.16). In particular, for small κ one has that

$$\begin{aligned}
&\sigma_{A0} \simeq \overline{\beta} + \phi\overline{R},\\
&(\sigma_{B0} - \sigma_{A0})/\varepsilon_L \propto 1/\phi,\\
&(\sigma_{A0} + \sigma_{C0})/2 = \mathrm{const},\\
&\varepsilon_{R\infty}/\varepsilon_L = \mathrm{const},\\
&\sigma_{A0} - \sigma_{A\infty} = \mathrm{const}.
\end{aligned}$$

These entail that the stress threshold σ_{A0} linearly increases and the hardening slope decreases (with constant $\sigma_{B0} - \sigma_{A0}$) with the crystallized proportion ϕ. On the other hand, the mid-loop stress $(\sigma_{A0}+\sigma_{C0})/2$, the ratio $\varepsilon_{R\infty}/\varepsilon_L$, and $\sigma_{A0}-\sigma_{A\infty}$ are independent of ϕ (to first order). An illustration of the corresponding material behavior for different values of the crystallization proportion is presented in Figure 8.

4.2. Mean crystal-grain size dependence.

The dependence on the mean crystal-grain radius r is included in the model by allowing a r-dependence of the parameters $(\overline{\beta}, \overline{H}, \overline{A}, \overline{h}, \overline{\varepsilon}_L, \overline{\kappa}, \overline{R})$. In particular, the free energy and the dissipation potential of the model in the present microstructure-dependent setting read, respectively

$$\begin{aligned}\Phi(\boldsymbol{\sigma}, \boldsymbol{e}^{\rm tr}, \boldsymbol{q}; \phi, r) = &-\frac{1}{2}\boldsymbol{\sigma} : \mathbb{C}^{-1}\boldsymbol{\sigma} - \boldsymbol{\sigma} : \boldsymbol{e}^{\rm tr} + \\ &+ \phi\overline{\beta}(r)\|\boldsymbol{e}^{\rm tr} - \boldsymbol{q}\| + \frac{\overline{h}(r)}{2}\|\boldsymbol{e}^{\rm tr}\|^2 - \overline{A}(r)\varepsilon^{\rm tr} : \boldsymbol{q} \\ &+ \frac{\overline{H}(r)}{2}\|\boldsymbol{q}\|^2 + I_{\phi\overline{\varepsilon}_L(r)}(\boldsymbol{e}^{\rm tr}),\end{aligned} \tag{4.2}$$

$$D(\dot{\boldsymbol{e}}^{\rm tr}, \dot{\boldsymbol{q}}; \phi, r) = \phi\overline{R}(r)\left(\overline{\kappa}^{-1}(r)\|\dot{\boldsymbol{q}}\| \vee \|\dot{\boldsymbol{e}}^{\rm tr}\|\right) \qquad \text{for } \overline{\kappa}(r) > 0. \tag{4.3}$$

Correspondingly, the yield function reads

$$F(\boldsymbol{X}, \boldsymbol{Q}; \phi, r) = \|\boldsymbol{X}\| + \overline{\kappa}(r)\|\boldsymbol{Q}\| + \phi\overline{R}(r).$$

The constitutive relations are obtained as in Section 2. The evolution of the material is driven by the inclusion

$$\partial_{(\dot{\boldsymbol{e}}^{\rm tr}, \dot{\boldsymbol{q}})} D(\dot{\boldsymbol{e}}^{\rm tr}, \dot{\boldsymbol{q}}; \phi, r) + \partial_{(\boldsymbol{e}^{\rm tr}, \boldsymbol{q})}\Phi(\boldsymbol{\sigma}, \boldsymbol{e}^{\rm tr}, \boldsymbol{q}; \phi, r) \ni \boldsymbol{0}. \tag{4.4}$$

We shall remark that no dynamics is presently associated to the parameters ϕ and r. These are here assumed as known, possibly being not constant. We plan to tackle the coupled evolution of ϕ and r elsewhere.

The explicit dependence of the parameters $(\overline{\beta}, \overline{H}, \overline{A}, \overline{h}, \overline{\varepsilon}_L, \overline{\kappa}, \overline{R})$ on r is phenomenological and is fitted on the observed mechanical behaviors in [11, 12]. We establish the crystal-grain size dependence of the parameters by enforcing equations (3.17) to (3.22) (or, whenever needed, (3.13a)). In particular, the threshold stresses σ_X and the residual strains $\varepsilon_{R0}, \varepsilon_{R\infty}$ are available for different values of the mean crystal-grain radius r.

In order to perform the fitting, some functional dependence form on r for the parameters has to be assumed. As for the stress thresholds σ_X we employ with the classical Hall-Petch law, which is commonly applied to yield stresses in the plasticity context. In particular, we let

$$\sigma_X = \sigma_X^0 + \frac{k_X}{\sqrt{r}}$$

Moreover, the following fitting are used for the maximal transformation strain and the plastic residual strains:

$$\varepsilon_L(r) = \overline{\varepsilon}_L(1 - a\exp(-b\sqrt{r})),$$
$$\varepsilon_{R\infty}(r) = \varepsilon_L(r)(\varepsilon_0 + c_-(\sqrt{r_0} - \sqrt{r})^+ + c_+(\sqrt{r} - \sqrt{r_0})), \qquad \varepsilon_{R0}(r) = d \cdot \varepsilon_{R\infty}(r)$$

In [11, 12] it is observed that the maximal transformation stress is $\overline{\varepsilon}_L \simeq 7.5\%$ and that there is an optimal grain radius $r_0 = 50$ nm at which the plastic residual strains are minimal. The fitting constants are in particular determined as

$$\overline{\varepsilon}_L = 7.5\%,$$
$$a = 8.5,\ b = 0.72\,\mathrm{nm}^{-1/2},\ \varepsilon_0 = 0.03,\ c_- = 0.044\ \mathrm{nm}^{-1/2},\ c_+ = 0.035,\ d = 0.2,$$
$$k_{A0} = 2 \cdot 10^3\ \mathrm{MPa} \cdot \mathrm{nm}^{1/2},\ \sigma_{A0}^0 = 0.42 \cdot 10^3\ \mathrm{MPa},$$
$$k_{B0} = 3.7 \cdot 10^3\ \mathrm{MPa} \cdot \mathrm{nm}^{1/2},\ (\sigma_{B0}^0 \equiv \sigma_{A0}^0),$$
$$k_{C0} = 5.8 \cdot 10^3\ \mathrm{MPa} \cdot \mathrm{nm}^{1/2},\ \sigma_{C0}^0 \simeq 0\ \mathrm{MPa},$$
$$k_{A\infty} = 0.8 \cdot 10^3\ \mathrm{MPa} \cdot \mathrm{nm}^{1/2},\ \sigma_{A\infty}^0 = 0.43 \cdot 10^3\ \mathrm{MPa}$$

and are then kept fixed for all simulations.

4.3. Time discretization

We are interested in finding solutions of the evolution problem (4.4) along with initial conditions $(\boldsymbol{e}_0^{\mathrm{tr}}, \boldsymbol{q}_0)$ and for a given stress and microstructure-parameter history

$t \in [0,\overline{t}] \mapsto (\boldsymbol{\sigma}(t),\phi(t),r(t)) \in \mathbb{R}^{3\times 3}_{\mathrm{sym}} \times [0,1] \times (0,\infty)$. This corresponds to the stress-controlled evolution at the material point along with an evolving microstructure. We proceed by time discretization: let us introduce a partition $0 = t_0 < t_1, \dots, < t_N = \overline{t}$ and sequentially find the solutions $(\boldsymbol{e}^{\mathrm{tr}}_{n+1}, \boldsymbol{q}_{n+1})$ of the minimization problems

$$\min_{\boldsymbol{e}^{\mathrm{tr}},\boldsymbol{q}} \left\{ D(\boldsymbol{e}^{\mathrm{tr}} - \boldsymbol{e}^{\mathrm{tr}}_n, \boldsymbol{q} - \boldsymbol{q}_n; \phi_{n+1}, r_{n+1}) + \Phi(\boldsymbol{\sigma}_{n+1}, \boldsymbol{e}^{\mathrm{tr}}, \boldsymbol{q}; \phi_{n+1}, r_{n+1}) \right\} \tag{4.5}$$

for $n = 0, \dots, N-1$, where the values $\boldsymbol{\sigma}_{n+1} = \boldsymbol{\sigma}(t_{n+1})$, $\phi_{n+1} = \phi(t_{n+1})$, and $r_{n+1} = r(t_{n+1})$ are known. The reader is referred to [5, 14] for the analogous treatment of the ARS model. The above minimum problem corresponds to the system

$$\partial_{(\dot{\boldsymbol{e}}^{\mathrm{tr}},\dot{\boldsymbol{q}})} D(\boldsymbol{e}^{\mathrm{tr}} - \boldsymbol{e}^{\mathrm{tr}}_n, \boldsymbol{q} - \boldsymbol{q}_n; \phi_{n+1}, r_{n+1}) + \partial_{(\boldsymbol{e}^{\mathrm{tr}},\boldsymbol{q})} \Phi(\boldsymbol{\sigma}_{n+1}, \boldsymbol{e}^{\mathrm{tr}}, \boldsymbol{q}; \phi_{n+1}, r_{n+1}) \ni \boldsymbol{0} \tag{4.6}$$

which in turn is the implicit Euler time discretization of the continuous constitutive equation (4.4).

Let us assume that the convexity condition (3.13a) holds for the r-dependent parameters $\overline{h}$, $\overline{H}$, $\overline{A}$ along all the evolution. Then, problems (4.5) reduce to uniform convex minimizations. As such, they admit a unique solution $\{(\boldsymbol{e}^{\mathrm{tr}}, \boldsymbol{q})\}_{n=0}^{N}$.

For the sake of simplicity, the actual computation of solution to (4.5) is performed on a suitably regularized version of the problem. Indeed, as both D and Φ are nonsmooth at the origin, one resorts in a regularization of some occurrences of the norms by means of a small regularization parameter $\delta > 0$ as $\|\boldsymbol{y}\|_\delta := \sqrt{\|\boldsymbol{y}\|^2 + \delta^2} - \delta$. This regularization is clearly beneficial for the stability of the underlying numerical algorithm. On the other hand it is essentially inconsequential with respect to the predicted mechanical behavior. In particular, it does not alter the uniform convexity of the energy and it can be checked that solutions to the regularized system converge uniformly to solution of the nonregularized one for $\delta \to 0$ by adapting the similar argument in [1].

For the sake of definiteness, let us restate here the nonlinear system (4.6) in comple-

mentary form as

$$\boldsymbol{X} = \boldsymbol{s} - \phi_{n+1}\overline{\beta}(r_{n+1})\frac{\boldsymbol{e}^{\rm tr} - \boldsymbol{q}}{\|\boldsymbol{e}^{\rm tr} - \boldsymbol{q}\|_\delta + \delta} - \overline{h}(r_{n+1})\boldsymbol{e}^{\rm tr} + \overline{A}(r_{n+1})\boldsymbol{q} - \gamma\frac{\boldsymbol{e}^{\rm tr}}{\|\boldsymbol{e}^{\rm tr}\|}, \tag{4.7a}$$

$$\boldsymbol{Q} = \phi_{n+1}\overline{\beta}(r_{n+1})\frac{\boldsymbol{e}^{\rm tr} - \boldsymbol{q}}{\|\boldsymbol{e}^{\rm tr} - \boldsymbol{q}\|_\delta + \delta} - \overline{H}(r_{n+1})\boldsymbol{q} + \overline{A}(r_{n+1})\boldsymbol{e}^{\rm tr}, \tag{4.7b}$$

$$\boldsymbol{e}^{\rm tr} = \boldsymbol{e}_n^{\rm tr} + z\frac{\boldsymbol{X}}{\|\boldsymbol{X}\|}, \tag{4.7c}$$

$$\boldsymbol{q} = \boldsymbol{q}_n + z\frac{\boldsymbol{Q}}{\|\boldsymbol{Q}\|_\delta + \delta}, \tag{4.7d}$$

$$F = \|\boldsymbol{X}\| + \overline{\kappa}(r_{n+1})\|\boldsymbol{Q}\|_\delta + \phi_{n+1}\overline{R}(r_{n+1}), \tag{4.7e}$$

$$\gamma \geq 0, \quad \|\boldsymbol{e}^{\rm tr}\| \leq \phi_{n+1}\overline{\varepsilon}_L(r_{n+1}), \tag{4.7f}$$

$$z \geq 0, \quad F \leq 0, \quad zF = 0. \tag{4.7g}$$

From the algorithmical viewpoint one proceeds as follows. At time t_{n+1} the yield function F is evaluated at the strains $\boldsymbol{e}_n^{\rm tr}$, $\boldsymbol{q}_n$ and current (given) stress $\boldsymbol{\sigma}_{n+1}$ and microstructure parameters (ϕ_{n+1}, r_{n+1}). If $F(\boldsymbol{\sigma}_{n+1}, \boldsymbol{e}_n^{\rm tr}, \boldsymbol{q}_n; \phi_{n+1}, r_{n+1}) \leq 0$, then one chooses $z = 0$, which implies $\boldsymbol{e}^{\rm tr} = \boldsymbol{e}_n^{\rm tr}$ and $\boldsymbol{q} = \boldsymbol{q}_n$. If on the contrary, $F(\boldsymbol{\sigma}_{n+1}, \boldsymbol{e}_n^{\rm tr}, \boldsymbol{q}_n; \phi_{n+1}, r_{n+1}) > 0$ then evolution of $(\boldsymbol{e}^{\rm tr}, \boldsymbol{q})$ occurs and one solves (4.7a)-(4.7d) together with $F = 0$ (see (4.7e) and (4.7g)). The nonnegativity of z in (4.7g) is not directly enforced and serves as a consistency test instead. The constraint (4.7f) is initially ignored (along with the γ-term in (4.7a)) and the system is solved via *fsolve* in MATLAB®. Then, the constraint $\|\boldsymbol{e}^{\rm tr}\| \leq \phi_{n+1}\overline{\varepsilon}_L(r_{n+1})$ is checked. If this test fails, the system is augmented by the equation $\|\boldsymbol{e}^{\rm tr}\| = \phi_{n+1}\overline{\varepsilon}_L(r_{n+1})$ and the unknown γ in (4.7a) and solved.

Alternatively to the a posteriori check of the constraint, one can introduce a penalization by replacing the indicator function $I_{\phi_{n+1}\overline{\varepsilon}_L(r_{n+1})}$ via

$$V_\delta(\boldsymbol{e}^{\rm tr}) = \frac{1}{2\delta}((\|\boldsymbol{e}^{\rm tr}\| - \phi_{n+1}\overline{\varepsilon}_L(r_{n+1}))^+)^2,$$

which provides the additional Lipschitz continuous contribution

$$-\frac{1}{\delta}(\|\boldsymbol{e}^{\rm tr}\| - \phi_{n+1}\overline{\varepsilon}_L(r_{n+1}))^+\frac{\boldsymbol{e}^{\rm tr}}{\|\boldsymbol{e}^{\rm tr}\|}$$

to the generalized thermodynamic force $\boldsymbol{X}$. This penalization is once again justified by the fact that for $\delta \to 0$ one can rigorously prove that the original constraint is recovered, see again [1].

Under suitable smoothness and compatibility assumptions on data and parameters, the continuous problem (4.4) can be proved to admit an *energetic solution* in the sense of [25, 27]. In particular, one can prove that as the diameter of the time-partition goes to zero (a suitable right-continuous interpolant of) the discrete solution $\{(\boldsymbol{e}^{\rm tr}, \boldsymbol{q})\}_{n=0}^{N}$ pointwise converges to a limiting trajectory $t \in [0, \overline{t}] \mapsto (\boldsymbol{e}^{\rm tr}(t), \boldsymbol{q}(t))$ fulfilling the initial condition as well as the *global stability* condition

$$\begin{aligned}\widehat{\Phi}(t) &:= \Phi(\boldsymbol{\sigma}(t), \boldsymbol{e}^{\rm tr}(t), \boldsymbol{q}(t); \phi(t), r(t)) \\ &\leq \Phi(\boldsymbol{\sigma}(t), \widehat{\boldsymbol{e}}^{\rm tr} - \boldsymbol{e}^{\rm tr} \boldsymbol{e}^{\rm tr}, \widehat{\boldsymbol{q}}; \phi(t), r(t)) + D(\widehat{\boldsymbol{e}}^{\rm tr} - \boldsymbol{e}^{\rm tr}(t), \widehat{\boldsymbol{q}} - \boldsymbol{q}(t); \phi(t), r(t)) \\ &\qquad \forall (\widehat{\boldsymbol{e}}^{\rm tr}, \widehat{\boldsymbol{q}}) \in \mathbb{R}^{3\times 3}_{\rm dev} \times \mathbb{R}^{3\times 3}_{\rm dev},\ t \in [0, T], \end{aligned} \tag{4.8}$$

and the *energy conservation*

$$\hat{\Phi}(t) + {\rm Diss}(\boldsymbol{e}^{\rm tr}, \boldsymbol{q}; [0, t]) = \hat{\Phi}(0) + \int_0^t P(s) {\rm d}s. \tag{4.9}$$

In the latter, the term ${\rm Diss}(\boldsymbol{e}^{\rm tr}, \boldsymbol{q}; [0, t])$ corresponds to the dissipated energy over $[0, t]$ and reads

$${\rm Diss}(\boldsymbol{e}^{\rm tr}, \boldsymbol{q}; [0, t]) = \sup \left\{ \sum_{i=0}^{N-1} D(\boldsymbol{e}^{\rm tr}(t_{n+1}) - \boldsymbol{e}^{\rm tr}(t_n), \boldsymbol{q}(t_{n+1}) - \boldsymbol{q}(t_n); \phi(t_{n+1}), r(t_{n+1})) \right\},$$

the supremum being taken over all partitions of $[0, t]$. The term P is instead the power of external actions. In particular,

$$P(t) = \Big(\partial_{\boldsymbol{\sigma}} \Phi : \dot{\boldsymbol{\sigma}} + \partial_\phi \Phi \dot{\phi} + \partial_r \Phi \dot{r} \Big) (\boldsymbol{\sigma}(t), \boldsymbol{e}^{\rm tr}(t), \boldsymbol{q}(t); \phi(t), r(t)).$$

Whenever the r-dependence of the parameters $\overline{\beta}, \overline{A}, \overline{H}, \overline{h}, \overline{\varepsilon}_L, \overline{R}$, and $\overline{\kappa}$ is such that the energy $\Phi(\boldsymbol{\sigma}, \cdot, \cdot; \phi, r)$ and the dissipation potential $D(\cdot, \cdot; \phi, r)$ remain uniformly coercive and smooth one can follow the general theory of energetic solvability [25] and obtain the existence of a trajectory solving (4.8)-(4.9). This particularly applies to all computations

of Subsections 4.4 and 4.5 where the microstructure parameters ϕ and r are assumed to be constant, for simplicity. In this special situation, the mentioned convergence result for time-discrete solutions can be directly inferred from the analysis of the ARS, see [14].

4.4. Uniaxial tests

We shall provide here some illustration of the model capability of reproducing the uniaxial experimental results of [11, 12]. Some biaxial computation is reported in Subsection 4.5 below. The computations are obtained by means of the time-discretization method of Subsection 4.3.

At first, we illustrate in Figure 8 the effect of different crystallized proportions on a cyclic tensile loading test with the choices $\overline{\kappa} = 0.02$, $\overline{\varepsilon}_L = 2\%$, $\overline{R} = 120$ MPa, $\overline{\beta} = 500$ MPa, $\overline{h} = 4 \cdot 10^3$ MPa, $\overline{A} = 10^4$ MPa, $\overline{H} = 10^5$ MPa (no dependence of the parameters on the mean crystal-grain radius is assumed, for simplicity). The assumption of a rather small transformation strain (2%) is consistent with a fine microstructure in the crystallized regions (10-20 nm) which can coexist with amorphous regions. For small ϕ, the nonlinear behavior of the material gets closer to be elastic. On the contrary, the maximal reorientation strain $|\varepsilon^{\rm tr}| = \overline{\varepsilon}_L = 2\%$ is obtained for the completely crystallized material $\phi = 1$.

We consider now the case where the material is nearly fully crystallized ($\phi \simeq 1$) and the mean grain-size is changing. We collect in Figure 9 the experimental results (left column) and the numerical simulations (middle and right columns) of the cyclic loading regime for five microstructural situations corrisponding to mean crystal radii $r = 30$, 50, 100, 350, 1000 nm. The numerical results in the central column are obtained through a fitting on the basis of Subsection 3.8 of the material parameters $(\varepsilon_L, \kappa, R, h, H, A)$ on the experimental data (threshold stresses and residual strains) pertaining each experimental situation. The right column records the results obtained by a single fit on the five experimental situations along the procedure described in Subsection 4.2. A good agreement between the experiments and the simulations is obtained. In particular, the

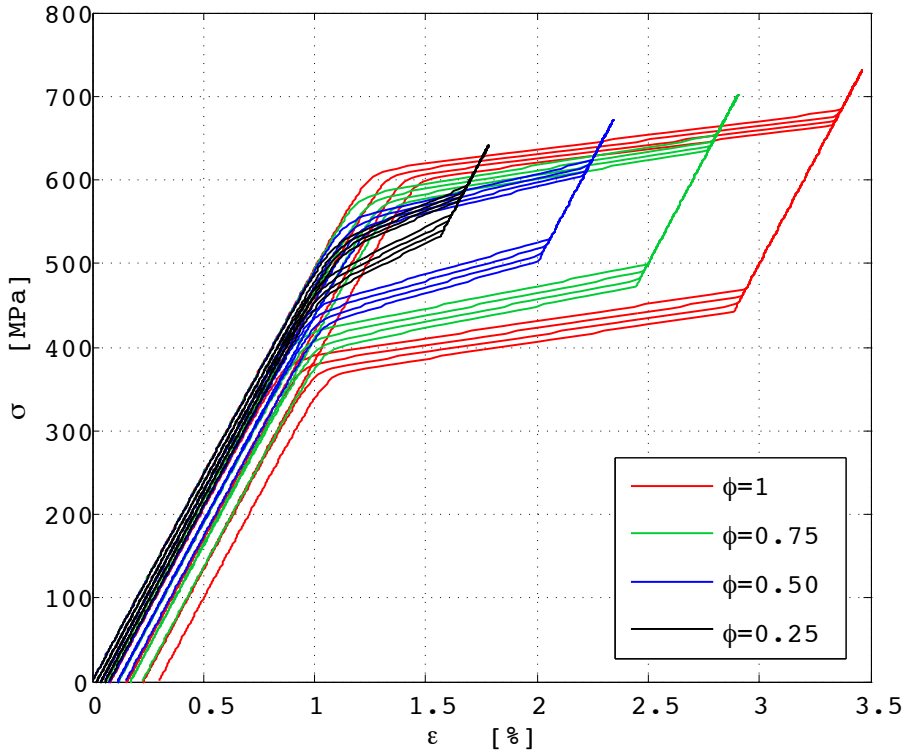

Figure 8: Cycles at varying ϕ.

emergence of permanent inelastic effects as well as the degradation of the material for large crystal grains is reproduced.

One has however to mention two undesirable features of the present approach. At first, in contrast with experiments the fatigue-induced stress drop $\Delta\sigma_B$ in the upper plateau is smaller than the drop $\Delta\sigma_C$ in the lower one. Secondly, the convexity requirement for the free energy leads to stronger hardening.

4.5. Biaxial tests

In order to illustrate the three-dimensional response of the model, we report here two examples of biaxial tests. Computations are performed along the same lines of Subsection 4.3 by using the fitted parameters from Subsection 4.2.

We will consider non-proportional hourglass-shaped tests in the plane-stress setting,

in which σ_{11} and σ_{12} are driven (in absolute value) to a maximum value σ_M greater than austenite-start stress σ_A. The stress history is here symmetric with respect to sign reversal of the stress components (note on the contrary that we considered only tension in the uniaxial case). In the biaxial test of Figure 10 the model parameters

$$\begin{aligned} &\varepsilon_L = 7 \cdot 10^{-2}, \quad \kappa = 0.087, \quad R = 200\,\text{MPa}, \quad \beta = 300\,\text{MPa}, \\ &h = 370\,\text{MPa}, \quad A = 1.6 \cdot 10^3\,\text{MPa}, \quad H = 7.3 \cdot 10^3\,\text{MPa} \end{aligned} \tag{4.10}$$

are used, the same of the uniaxial test in Fig. 9, middle column, 5^{th} row. The strain response during the first cycle is shown on the right. The circles mark the time discrete steps, corresponding to fixed stress increments. The rapidly changing strain dynamics indicates the transformation. The strain evolution for the first half-cycle (in which σ_{12} varies from 0 to σ_M and then again to 0) corresponds to the upper part of the diagram. The emergence of a residual strain $\varepsilon_{12} = \gamma_{12}/2 > 0$ can be detected, whereas the residual strain ε_{11} is approximately vanishing. At the end of the entire first cycle, two (small) residual strain components $\varepsilon_{12} < 0, \varepsilon_{11} > 0$ can be observed.

The strain dynamics for similar non-proportional hourglass-shaped tests are shown in Figure 11 for the two different parameter set, namely the choice (4.10) and the second set

$$\begin{aligned} &\varepsilon_L = 6 \cdot 10^{-2}, \quad \kappa = 3.7 \cdot 10^{-3}, \quad R = 240\,\text{MPa}, \quad \beta = 410\,\text{MPa}, \\ &h = 3 \cdot 10^3\,\text{MPa} \quad A = 5 \cdot 10^4\,\text{MPa} \quad H = 9.5 \cdot 10^5\,\text{MPa}. \end{aligned} \tag{4.11}$$

which corresponds to the 2^{nd} row of Fig. 9. On the left of Figure 10 parameters are fitted with respect to the case of relatively large crystal grains as in the last experiment on the left of in Figure 9. The parameter set (4.11) corresponds to the second experiment on the left of in Figure 9, that is the one that corresponds to the optimal microstructure. As expected, the fatigue effects are evident in the first case while they are essentially negligible in the second one.

5. Conclusions

We have presented an extension of the model in [5] in the direction of describing the microstructure-dependent permanent inelastic effects in mechanical tests induced by cycling fatigue. The detailed analysis of the uniaxial tension case has been devised in order to relate the model parameters with the observable mechanical effects. On the base of this analysis, an effective calibration strategy for material parameters from experimental cyclic tests has been presented. Moving from recent experimental evidence [9, 11], degradation effects relating fatigue and microstructural features, such as crystalized fraction and mean grain size, have been examined. The new modeling proposition results from simple and experimentally accessible assumptions on the microstructural dependence of material parameters. The mathematical setting as well as its numerical simulation is discussed. In particular, numerical tests in both the uniaxial and the biaxial case are performed and the experimental behavior is compared with the numerical outcomes.

Acknowledgement

We would like to express our gratitude to the Authors of [9, 10, 11, 12] for providing us the experimental data and especially to Petr Šittner for many inspiring conversations on these topics. This work has been supported by the ERC-FP7-IDEAS-StG Grant #200497 *BioSMA* and the IMATI-CNR.

[1] F. Auricchio, A. Mielke, U. Stefanelli, *A rate-independent model for the isothermal quasi-static evolution of shape-memory materials*. Math. Models Meth. Appl. Sci. **18** (2008), 125-164.

[2] F. Auricchio, L. Petrini, *Improvements and algorithmical considerations on a recent three- dimensional model describing stress-induced solid phase transformations*, Internat. J. Numer. Methods Engrg. **55** (2002), 1255-1284.

[3] F. Auricchio, L. Petrini, *A three-dimensional model describing stress-temperature induced solid phase transformations. Part I: Thermomechanical coupling and hybrid composite applications*, Internat. J. Numer. Methods Engrg. **61** (2004), 716-737.

[4] F. Auricchio, L. Petrini, *A three-dimensional model describing stress-temperature induced solid phase transformations. Part II: Solution algorithm and boundary value problems*, Internat. J. Numer. Methods Engrg. **61** (2004), 807-836.

[5] F. Auricchio, A. Reali, U. Stefanelli, *A three-dimensional model describing stress-induced solid phase transformation with permanent inelasticity*, Int. J. Plasticity **23** (2007), 207-226.

[6] F. Auricchio, A. Reali, U. Stefanelli, *A macroscopic 1D model for shape memory alloys including asymmetric behaviors and transformation-dependent elastic properties*, Comput. Methods Appl. Mech. Engrg. **198** (2009), 1631-1637.

[7] N. Barrera, P. Biscari, M.F. Urbano, *Macroscopic modeling of functional fatigue in shape memory*, Eur. J. Mech. A Solids (2014), to appear.

[8] Z. Bo, D.C. Lagoudas, *Thermomechanical modeling of polycrystalline SMAs under cyclic loading. Part III: evolution of plastic strains and two-way shape memory effect*, Int. J. Eng. Sci. **37** (1999), 1175-1203.

[9] B. Malard, J. Pilch, P. Sittner, D. Schryvers, V. Gartnerova, R. Delville, D. Schryvers, C. Curfs, *Microstructure and functional property changes in thin Ni-Ti wires heat treated by electric current - High energy X-ray and TEM investigations*, Functional Materials Letters **2** (2009), 45-54.

[10] R. Delville, B. Malard, J. Pilch, P. Sittner, D. Schryvers, *Transmission electron microscopy investigation of dislocation slip during superelastic cycling of Ni-Ti wires*, Int. J. Plasticity **27** (2011), 282-297.

[11] B. Malard, J. Pilch, P. Sittner, R. Delville, C. Curfs, *In situ investigation of the fast microstructure evolution during electropulse treatment of cold drawn NiTi wires*, Acta Mater. **59** (2011), 1542-1556.

[12] R. Delville, B. Malard, J. Pilch, P. Sittner, D. Schryvers, *Microstructure changes during non-conventional heat treatment of thin Ni-Ti wires by pulsed electric current studied by transmission electron microscopy*, Acta Mater. **58** (2010), 4503-4515.

[13] T. W. Duerig, A. R. Pelton (Eds.), *SMST-2003 Proceedings of the International Conference on Shape Memory and Superelastic Technology Conference*, ASM International, 2003.

[14] M. Eleuteri, L. Lussardi, U. Stefanelli, *A rate independent model for permanent inelastic effects in shape memory materials*, Netw. Heterog. Media **6** (2011), 145-165.

[15] M. Frémond, *Non-Smooth Thermomechanics*, Springer-Verlag, Berlin, 2002.

[16] H. Funakubo (Ed.), *Shape Memory Alloys* Gordon and Breach Science Publishers, New York, 1987.

[17] K. Gall, H.J. Maier, *Cyclic deformation mechanisms in precipitated NiTi shape memory alloys*, Acta Mater **50** (2002), 4643-4657.

[18] D. Grandi, U. Stefanelli, *The Souza-Auricchio model for shape-memory alloys*, Preprint IMATI-CNR (2013), 12PV13/10/0.

[19] B. Halphen, Q. S. Nguyen, *Sur les matériaux standards généralisés*, J. Mécanique **14** (1975), 39-63.

[20] D.J. Hartl, D.C. Lagoudas, *Constitutive modeling and structural analysis considering simultaneous phase transformation and plastic yield in shape memory alloys*. Smart. Mater. Struct. **18** (2009), 104017-17pp.

[21] D.J. Hartl, G.C. Chatzigeorgiou, D.C. Lagoudas, *Three-dimensional modeling and numerical analysis of rate-dependent irrecoverable deformation in shape memory alloys*. Int. J. Plasticity **26** (2010), 1485-1507.

[22] D.C. Lagoudas, P. Entchev, *Modeling of transformation-induced plasticity and its effect on the behavior of porous shape memory alloys. Part I: constitutive model for fully dense SMAs*, Mech. Mater. **36** (2004), 865-892.

[23] Ch. Lexcellent, *Shape-Memory Alloys Handbook*, Wiley, 2013.

[24] S. Manchiraju, P.M. Anderson, *Coupling between martensitic phase transformations and plasticity: A microstructure-based finite element model*. Int. J. Plasticity **26** (2010), 1508-1526.

[25] A. Mielke, *Evolution in rate-independent systems (ch. 6)*, in C. Dafermos and E. Feireisl (Eds.) *Handbook of Differential Equations, Evolutionary Equations* **2** (2005), 461-559. Elsevier.

[26] A. Mielke, T. Roubíček, U. Stefanelli, Γ*-limits and relaxations for rate-independent evolutionary problems*, Calc. Var. Partial Differential Equations **31** (2008), 387416.

[27] A. Mielke, F. Theil, *On rate-independent hysteresis models*, NoDEA Nonlinear Differential Equations Appl. **11** (2004), 151-189.

[28] A. Paiva, M. Savi, A. Braga, P. Pacheco, *A constitutive model for shape memory alloys considering tensile-compressive asymmetry and plasticity*, Int. J. Solids Struct. **42** (2005), 3439-3457.

[29] K. Otsuka, C.M. Wayman (Eds.), *Shape Memory Materials*, Cambridge University Press, 1998.

[30] J. Otubo, F.C. Nascimento, P. Mel, L. Cardoso, M.J. Kaufman, *Influence of austenite grain-size on mechanical properties of stainless SMA*, Mater. Trans. **5** (2002), 916-919.

[31] D. Song, G. Kang, Q. Kan, C. Yu, C. Zhang, *The effect of martensite plasticity on the cyclic deformation of super-elastic NiTi shape memory alloy*. Smart. Mater. Struct. **23** (2014), 015008 -7pp.

[32] A.C. Souza, E.N. Mamiya, N. Zouain, *Three-dimensional model for solids undergoing stress-induced tranformations*, Eur. J. Mech. A Solids **17** (1998), 789-806.

[33] C. Yu, G. Kang, D. Song, Q. Kan, *Micromechanical constitutive model considering plasticity for super-elastic NiTi shape memory alloy*. Comp. Mater. Sci. **56** (2012), 1-5.

[34] C. Yu, G. Kang, Q. Kan, D. Song, *A micromechanical constitutive model based on crystal plasticity for thermo-mechanical cyclic deformation of NiTi shape memory alloys*. Int. J. Plasticity **44** (2013), 161-191.

[35] W. Zaki, Z. Moumni, *A 3D model of the cyclic thermomechanical behavior of shape memory alloys*. J. Mech. Phys. Solids **55** (2007), 2427-2454.

[36] W. Zaki, S. Zamfir, Z. Moumni, *An extension of the ZM model for shape memory alloys accounting for plastic deformation*. Mech. Mater. **42** (2010), 266-274.

[37] H. Zhang, X. Li, X. Zhang, *Grain-size-dependent martensitic transformation in bulk nanocrystalline*

TiNi under tensile deformation, J. Alloy Compd. **544** (2012), 19-23.

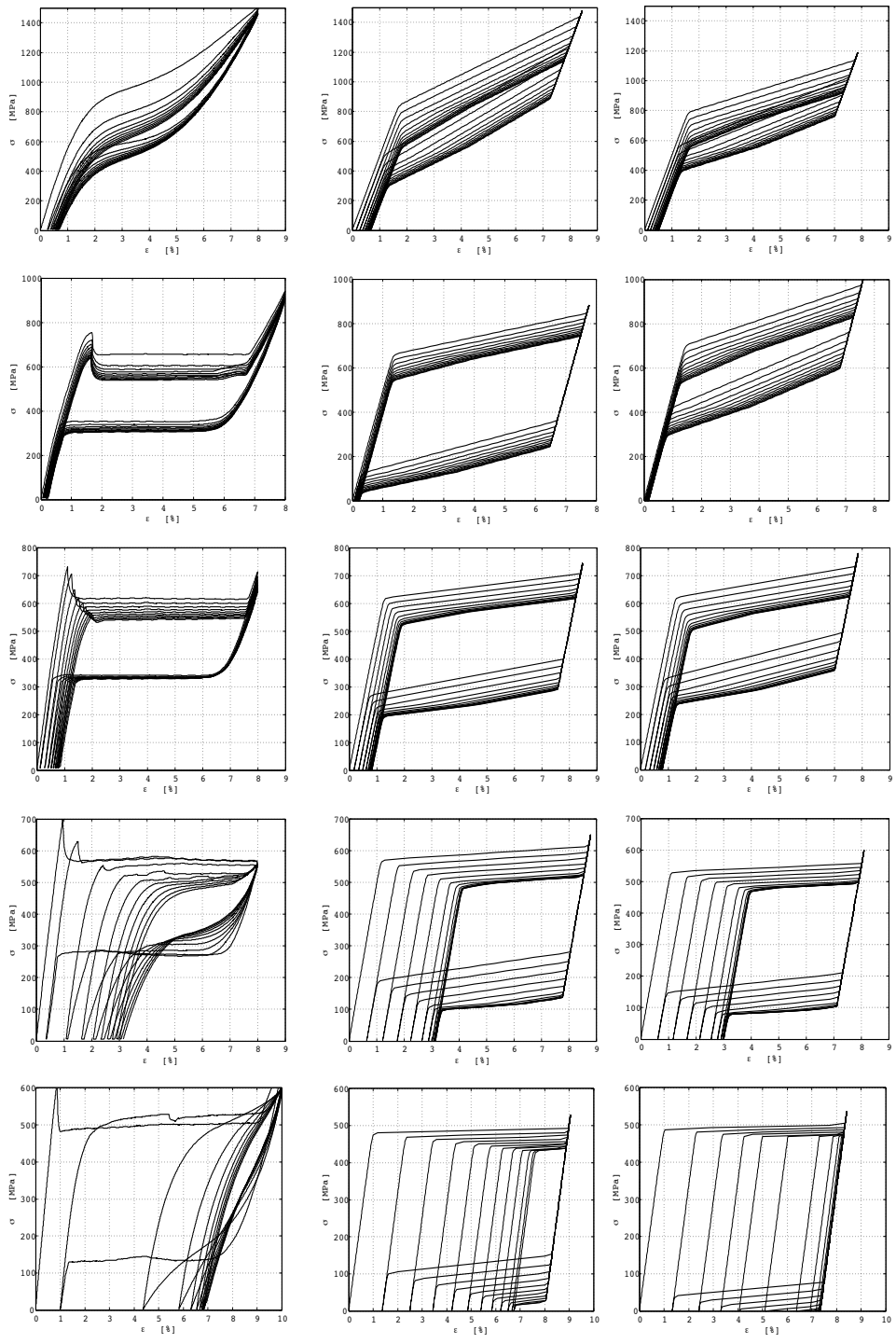

Figure 9: Comparison between experiments (left) and computations (middle and right) for mean crystal-grain radii $r = 30,\ 50,\ 100,\ 350.\ 1000$ nm (from top). The middle column corresponds to five separate fits, one for each experiment, whereas the right column arises from an overall fitting procedure.

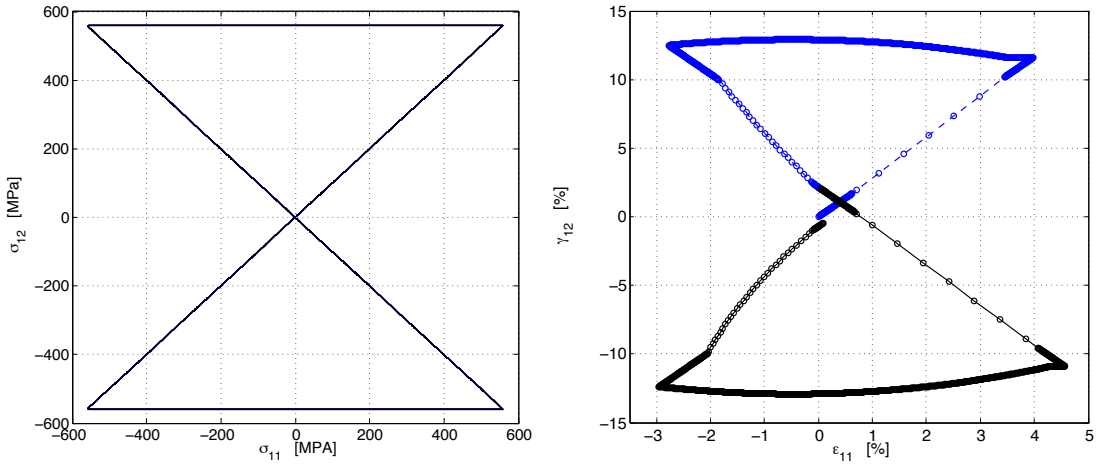

Figure 10: Biaxial non-proportional hourglass-shaped stress history (left) and first cycle strain output (right).

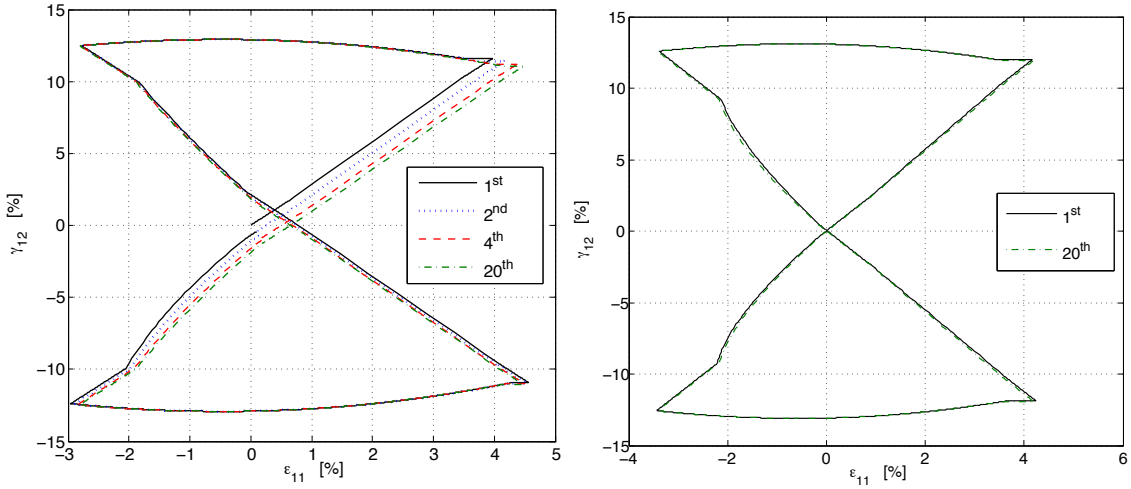

Figure 11: Biaxial non-proportional hourglass-shaped tests with material parameters sets (4.10) (left) and (4.11) (right). The evolution of the material response is displayed through twenty cycles.